3.23 Metal Fuel Performance Modeling and Simulation

T. Ogata
Central Research Institute of Electric Power Industry, Komae, Tokyo, Japan
Yeon Soo Kim and A. M. Yacout
Argonne National Laboratory, Argonne, IL, USA

Abbreviations

CDF	Cumulative damage function
CRIEPI	Central Research Institute of Electric Power Industry
FCR&D	Fuel Cycle Research and Development
FGR	Fission–gas–release
FP	Fission products
HIP	Hot isotropic pressing
ID	Inner-diameter
LA	Lanthanides
MA	Minor actinides
NRC	Nuclear Regulatory Commission
OD	Outer-diameter
PIE	Post irradiation examination

RED	Radiation-enhanced diffusion
SD	Smear density
WDS	Wavelength dispersive spectroscopy

3.23.1 Introduction

Metal fuel utilizing U–Pu–Zr or U–Zr alloys is one of the fast reactor fuel forms that is being developed extensively. In this chapter, the authors present the current status of modeling and simulation of metal fuel irradiation behavior at the continuum level.

For a brief introduction, the structure of a metal fuel pin and the main features of irradiation behavior are outlined.

The structure of a metal fuel pin is illustrated schematically in **Figure 1**. A cast U–Pu–Zr or U–Zr fuel alloy rod (fuel slug) is encapsulated in a steel tube (cladding). The gap between the fuel slug and cladding is filled with sodium, which is called bond-sodium. The ratio of the cross-sectional area of the fuel slug to that inside the cladding (fuel smear density) is typically adjusted to 75%. A relatively large space is provided in the upper half of the cladding (gas plenum) to suppress the excessive increase in the internal pressure due to fission gas accumulation.

The various phenomena caused by neutron irradiation in metal fuel are summarized in **Figure 2**, which shows the reported irradiation test results (e.g., Hofman and Walters,[1] see **Chapter 3.01, Metal Fuel**). During irradiation, fission gas atoms produced in the fuel slug agglomerate and form gas bubbles.
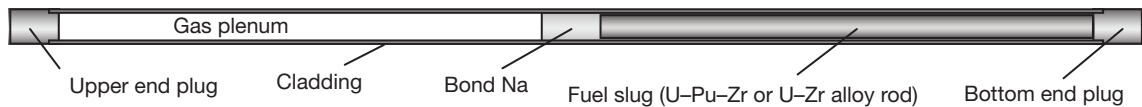

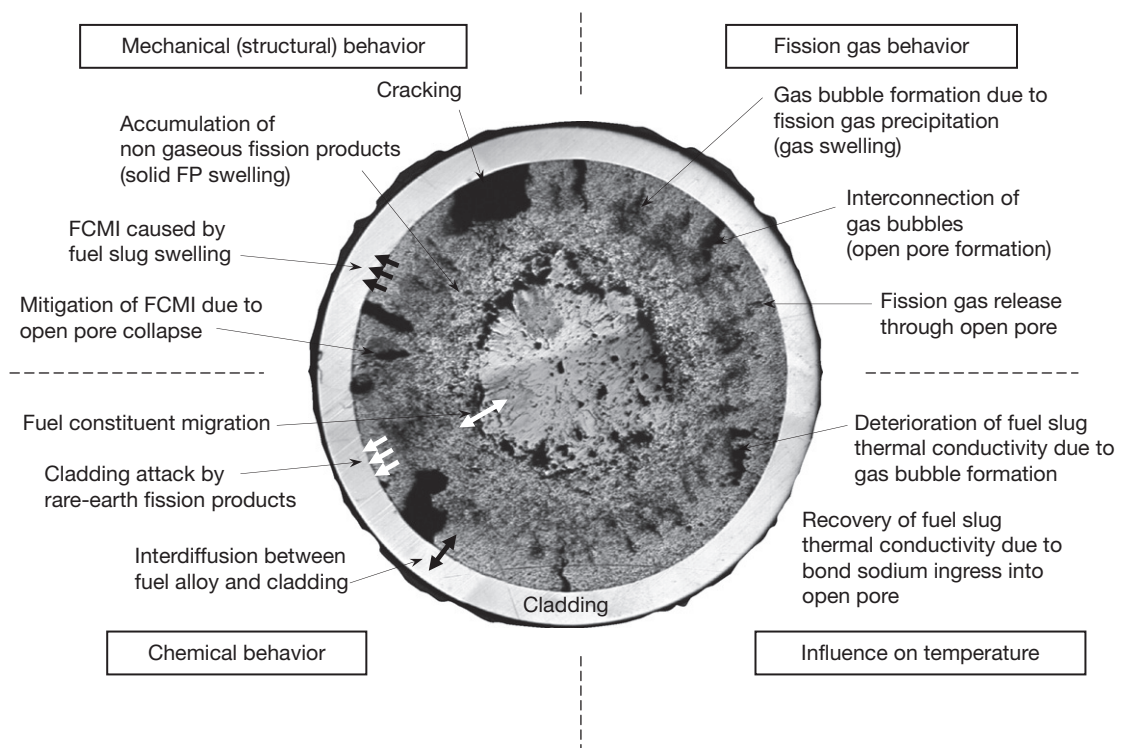**Figure 1**   Schematic view of metal fuel pin.

Figure 2   Outline of irradiation behavior of metal fuel.

In the peripheral region of the slug, where the temperature is relatively low, cavitation may occur because of anisotropic irradiation growth of the grains of the fuel alloy. Radial cracks may also take place at the U–Pu–Zr fuel slug surface. Gas bubble formation, cavitation, and crack formation cause swelling of the fuel slug and deteriorate its effective thermal conductivity. Fuel slug swelling narrows the gap between the slug and cladding, and a part of the bond-sodium at the gap is squeezed out to the gas plenum region. Continuing neutron irradiation grows the gas bubbles, and enhances formation of cavities and cracks (collectively called 'pores'). Coalescence among the pores may also occur, resulting in enlargement of the pores. The fuel slug swells further and comes into contact with the cladding at 1–2 at.% burnup. The progression of coalescence among the pores may cause formation of the open pores that are connected to the outside of the slug. Through the open pores, fission gas comes outside and the bond-sodium goes into the slug. The released fission gas accumulates in the gas plenum and increases its internal pressure. The ingression of bond-sodium recovers the effective thermal conductivity of the slug. The swollen fuel slug is restrained and compressed by the cladding, while it pushes out the cladding. This action–reaction is called fuel–cladding mechanical interaction (FCMI). The compressive stress applied to the swollen slug causes decrease in the open pore volume, which relaxes FCMI. Further irradiation leads to an unignorable level of fuel volume increase due to accumulation of nongaseous fission products (FPs), which is called 'solid fission product swelling.'

The cross-section of the irradiated fuel slug usually displays a few distinctive annular zones characterized by differences in fuel microstructure, particularly in size and number densities of pores. The annular zone formation may lead to changes in the radial distributions of the heat generation rate and effective thermal conductivity, both of which affect the fuel slug temperature distribution.

Thermochemical migration of U, Pu, and Zr in their distinctive directions established by radial multiphase fields and the temperature gradient causes their radial redistribution, which is known as 'constituent migration' or 'constituent redistribution.' Zr tends to gather at the fuel center region where bcc solid solution (γ-phase) emerges for a typical metal fuel pin, while U moves in the opposite direction. Pu does not migrate remarkably. The constituent migration affects local solidus temperature and thermal conductivity of the slug.

Rare-earth FPs move to the fuel slug surface and react with cladding. This reaction, called fuel–cladding chemical interaction (FCCI), reduces the effective thickness of the cladding and increases the local cladding stress. In the metal fuel design, FCCI is one of the life-limiting factors along with the plenum gas pressure rise.

The design and safety analysis of metal fuel pins require an understanding of the irradiation behavior and a quantitative evaluation of its influence on the margin to fuel pin failure. The modeling and simulation of the irradiation behavior provide the basis for them. The various phenomena in a metal fuel pin during irradiation are, as described earlier, interlinked directly or indirectly. The comprehensive understanding of irradiation behavior needs appropriate modeling of the respective phenomena and the relationship among them. When a specific phenomenon is examined in detail, a stand-alone model is often made, omitting the relation to the other phenomena under appropriate assumptions. In the irradiation behavior analysis for fuel pin design, the phenomena having limited influence on the other phenomena can be treated by simplified models.

Comprehensive simulation of steady-state irradiation behavior of metal fuel is usually performed with a computer code such as LIFE-METAL,[2] ALFUS,[3] MACSIS,[4] and FEAST-METAL.[5] Stand-alone models have been developed for constituent migration,[6] gas swelling, and cavitation[7] (see **Chapter 3.20, Modeling of Fission-Gas-Induced Swelling of Nuclear Fuels**). In this chapter, a model for constituent migration and computer codes LIFE-METAL and ALFUS are described as examples of metal fuel modeling and simulation.

3.23.2 Models for Constituent Migration

3.23.2.1 Introduction

One characteristic phenomenon of U–Zr or U–Pu–Zr metallic fast reactor fuel during irradiation is the migration of fuel constituents, which turns the uniform as-fabricated alloy into a locally heterogeneous fuel. This changes the properties locally and affects almost all other fuel behaviors.

For U–Pu–Zr metallic nuclear fuels, this phenomenon was first observed by Murphy *et al.*[8] They reported that irradiated U–Pu–Zr fuel rods showed three concentric microstructural zones containing

different U and Zr concentrations in each zone, suggesting that the change in composition was due to Zr migration. Later, Harbur et al.[9] found that an out-of-pile annealing produced constituent redistribution, indicating that a thermal gradient alone could generate a driving force sufficient for constituent redistribution (i.e., Soret-type migration). During the course of the integral fast reactor (IFR) fuel development program, extensive irradiation tests were carried out for U-based alloy fuels in which constituent redistribution was characterized (see Pahl et al.[10–12] and **Chapter 3.01, Metal Fuel**).

The typical as-fabricated U–Pu–Zr is shown in **Figure 3** together with constituent distributions. Fuel alloy is a mixture of three phases in this case. The concentration profiles are locally heterogeneous because of the individual phases. However, in the long range, it is marginally homogeneous without systematic changes in the concentrations.

As shown in **Figure 4**, the microstructures of the irradiated fuels commonly exhibit three distinct concentric zones, namely, a Zr-enriched central zone, a Zr-depleted and U-enriched intermediate zone, and a slightly Zr-enriched zone on the outer periphery. The annular zone structure was due not only to local compositions, but also to differences in porosity. Each annular zone lying in a different phase has different fuel swelling, specifically different gas bubble growth, which is the cause of the different pore morphology for each zone.

The reduction in Zr concentration in the mid-radius region lowers the fuel melting point, whereas the increase in Zr concentration in the fuel center

(a)   T179 irradiated to 2% burnup

(b)   DP-16 irradiated to 11% burnup
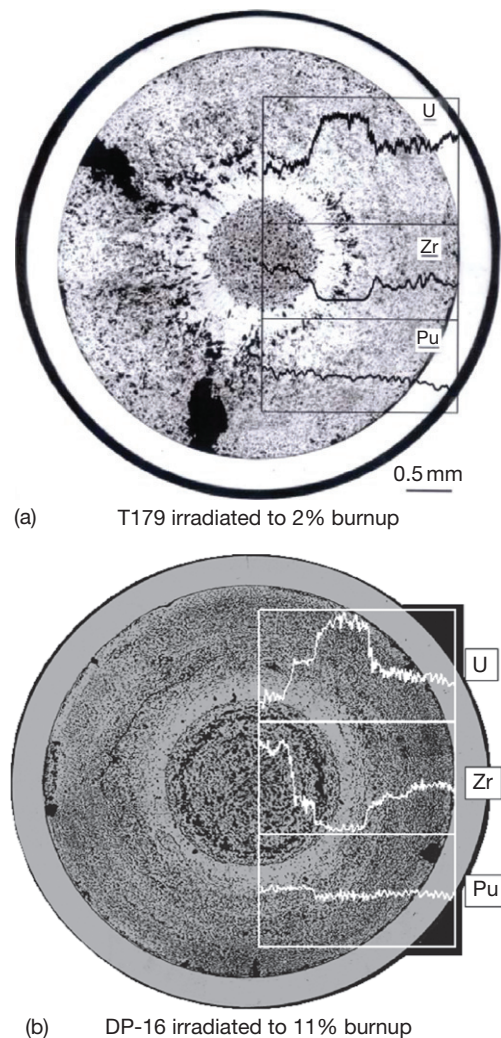
Figure 4 Cross-sectional optical photomicrograph of the postirradiation fuel and electron probe microanalysis (EPMA) scans. The fuel elements shown here were irradiated at similar temperatures in the EBR-II. (a) T179 irradiated to 2% burnup and (b) DP-16 irradiated to 11% burnup.
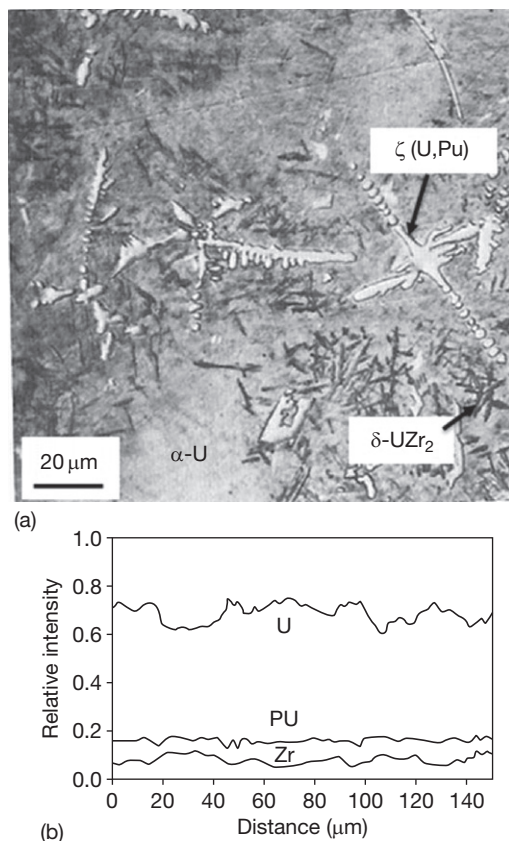

(a)

(b)

Figure 3 Characterization of injection casted U–15Pu–10Zr. (a) Optical micrograph of as-cast U–15Pu–10Zr (etched) and (b) Concentration profiles (EPMA).

increases fuel melting point there. This is fortuitous because the possibility of fuel melting is the highest in the fuel center region. Zr migration to the fuel surface is sometimes evident by the presence of a Zr-rich rind, which plays a positive role against FCCI.

Despite some irregularities, in general, the U profile is opposite to that of Zr, suggesting that U and Zr interdiffuse. The Pu concentration profile shows that it remained virtually unchanged. Although Pu migration itself is negligible, the presence of Pu in the alloy above 8 wt% enhanced the migration of other components. As suggested by Porter *et al.*,[12] this may be related to the increase in the gas bubble swelling rate in the high-Pu content fuels. The elevated temperature in high-porosity fuel is also a condition favorable for constituent migration. This hypothesis is supported by the observation that the constituent redistribution tends to saturate at a burnup of only a few atomic percent, when rapid initial gas-driven swelling results in an interconnected network of open porosity that releases most of the fission gases subsequently generated and greatly slows continued fuel swelling.

The underlying driving forces for constituent migration are as follows:

1. temperature gradients in the fuel,
2. solubility gradients in a phase and phase boundaries, and
3. additional chemical potentials applied by fuel–cladding gap and cladding.

The fuel's ever-present thermal gradients generate heat fluxes. To compensate for the heat flux, one of the fuel constituents, in this case Zr atoms, moves in the direction opposite to that of the heat flux. Because the heat flux is in the radial positive direction, the Zr atoms move to the fuel center. This is also known as the Soret-type migration. In modeling, this effect is quantitatively measured by the phenomenological property of 'heat of transport.' In a typical fuel, the axial migration is not observed primarily because the thermal gradients in this direction are much smaller (approximately two orders of magnitude smaller) than those in the radial direction.

Meanwhile, the poly-phase fields associated with the U–Zr and U–Pu–Zr alloy provide a driving force for constituent migration. The solubility of the solute atoms changes across the phase fields, and therefore, more precipitation occurs in some phases than in others, and within a phase field, the solubility of a species varies by the temperature distribution. This produces a concentration gradient in the continuous

phase, a phase that provides a medium for species to diffuse. An example can be found in **Figure 3**, where the α-U phase is the continuous phase. Fick's diffusion is driven by the concentration gradient.

In a metallic fuel, Zr affinity for nitrogen and oxygen also drives Zr migration to fuel surface if nitrogen and oxygen are present in the gap included during fabrication.

The migration tends to decrease and eventually stop with burnup because the concentration gradient generates a driving force for back diffusion. The observed redistribution is a balance between these driving forces. The fuel morphology irradiated to 11 at.% shown in **Figure 4(b)** shows only a slight difference from the one irradiated to 2 at.% shown in **Figure 4(a)**. This supports the prediction that migration quickly levels off early in life after a new distribution settles.

3.23.2.2 Phase Diagram

The ternary phase diagrams of U–Pu–Zr are available.[13] However, these ternary diagrams are not used in the kinetic models; instead a pseudo-binary diagram is used to simplify modeling with reasonable accuracy. CALPHAD thermodynamic assessment[14] of the pseudo-binary phase diagram shown in **Figure 5** was performed, based on the slightly modified results published in Kurata[15] and the application of the Thermo-Calc software by Andersson *et al.*[16] (see **Chapter 2.05, Phase Diagrams of Actinide Alloys**).

The complexity of the lower-Zr side in the phase diagram poses a challenging obstacle in modeling in that it is involved with the Zr-depleted fuel zone at an intermediate radius. In particular, the existence of the ζ-phase seems to cause additional difficulty in modeling. Unfortunately, the thermodynamic properties of this fuel phase are not known. The phase diagram shown in **Figure 5** is still too complex to be implemented in a model. A simplified phase diagram shown in **Figure 6** that still preserves the essential properties has been used. The main features of the simplification are twofold. First, the phases on the U + Pu-rich side were simplified by using the (α + ζ)- and (β + ζ)-phases for this region. (α + ζ) and (β + ζ) are pseudo-single phases that possess characteristics of the mixture of α and ζ, and β and ζ, respectively. Second, the sloped phase boundaries between the large-phase fields of ζ + γ, ζ + δ + γ, ζ + δ, and α + ζ + δ are approximated by parallel lines to the x-axis.

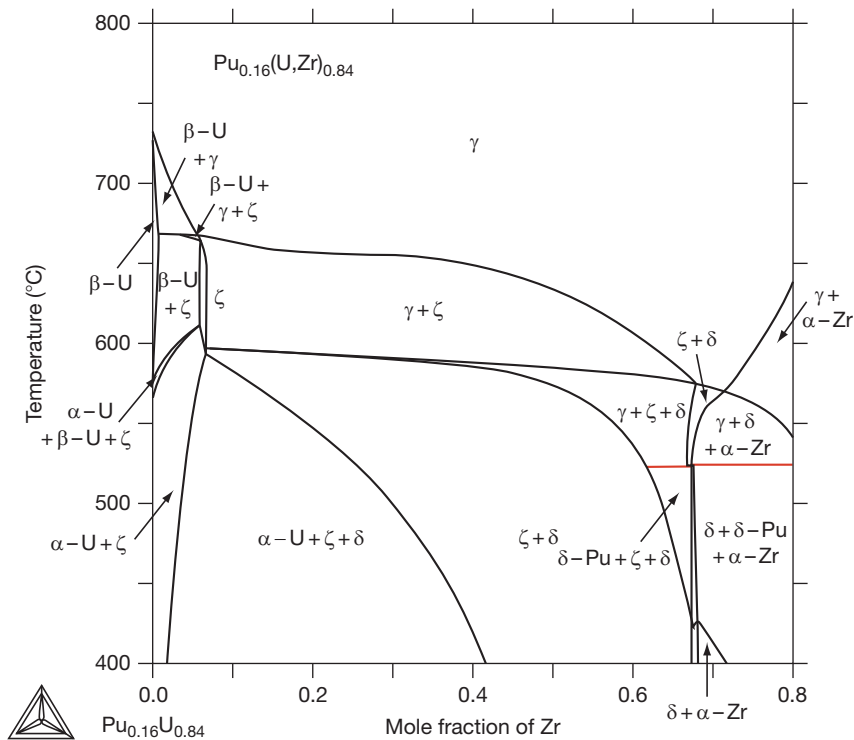When applied to a fuel with different Pu content, the phase diagram must be modified accordingly.

Figure 5   Pseudo-binary (U–Pu)–Zr phase diagram for the fixed Pu content at 19 wt%.
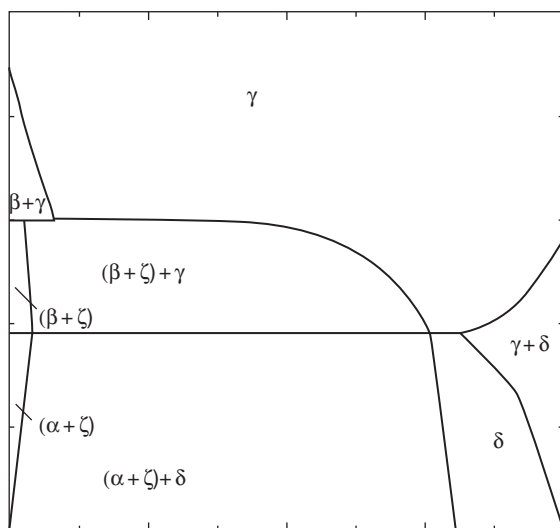

Figure 6   Simplified pseudo-binary phase diagram of U–19Pu–10Zr.

In particular, the temperatures at the phase boundaries between $\gamma_1 + \gamma_2$ and $(\beta + \zeta) + \gamma$ and between $(\beta + \zeta) + \gamma$ and $(\alpha + \zeta) + \delta$ must be changed. For example, if the Pu content decreases from the typical content of 19 wt% to 15 wt%, the phase boundary temperatures will slightly increase (by ~20 °C). For most cases, however, the Pu content is close to 19 wt%, so that the phase diagrams shown in **Figure 5** and in turn those shown in **Figure 6** can be applied without any modifications.

3.23.2.3   Temperature Prediction

Temperature is one of the most important factors that affect fuel constituent redistribution. Therefore, modeling constituent redistribution calls for a reliable prediction of fuel temperatures. Fuel temperature is affected by the thermal conductivity of the fuel, which in turn is changed by porosity evolution in the fuel matrix and sodium logging into open pores, in addition to changes in Zr concentration.

Porosity growth in U–Pu–Zr fuel during irradiation differs by zone. Typically, the central region with the γ-phase has relatively small pores that are formed by agglomeration of fine fission gas bubbles. The intermediate-radius region has the smallest pores, which are generally spherical. The pores in the fuel periphery, where the α-U and δ-phases are dominant, are different in morphology. These are most abundant in fraction and are generally nonspherical

because of swirling swelling. After fuel–cladding contact occurs, porosity tends to saturate because of swelling of solid FPs. Therefore, beyond ∼1 at.% burnup, porosity distribution is considered unchanged.

Porosity decreases fuel thermal conductivity, increasing fuel temperatures. However, in a fuel pin with a liquid-sodium bonded gap, subsequent sodium logging in the open pores improves fuel thermal conductivity. The effect of porosity formation on overall fuel thermal performance is a complicated topic for modeling. Model predictions of evolution of porosity in DP-16 with burnup are shown in **Figure 7**.

A model for the thermal conductivity reduction due to porosity and sodium logging into fuel porosity is reported by Bauer and Holland.[17] The reduction factor for fuel thermal conductivity by pores that are free of sodium logging, applicable to the central and intermediate zones where no sodium logging occurs, is given by

$$f_{p} = (1 - p)^{1.5\varepsilon} \qquad [1]$$

where ε is 1.72 for metallic fuel and p is the porosity fraction.

Liquid sodium, filled in the as-fabricated fuel–cladding gap, infiltrates into open pores in the fuel as fuel volume increases by swelling and increases the overall fuel thermal conductivity above that of the fuel alloy, depending on the available porosity. The effect of sodium infiltration is modeled also by using the Bauer–Holland model in the pores. The thermal conductivity of fuel during irradiation is expressed as follows:

$$f_{p-Na} = \left[1 - 3 \cdot \frac{1 - k_{Na}/k_f}{2/\varepsilon + (3 - 2/\varepsilon)(k_{Na}/k_f)} \cdot \frac{p_{Na}}{1 - p_g} \right] \quad [2]$$

where ε is 1.72, k_{Na} and k_f are thermal conductivities of liquid sodium and metallic fuel, respectively, and p_{Na} and p_g are fractions of porosity with and without sodium logging, respectively.

The sodium fraction in the pores reaches a maximum of 80% at the fuel periphery. Based on the typical fuel fabrication and operation parameters given in **Table 1**, fuel temperature predictions for DP-16 pin at several burnup points are shown in **Figure 8**. Fuel temperatures generally decrease with burnup as the power decreases, including the fuel surface temperature.

No discernable changes at the zone boundaries can be seen. Sodium logged in the periphery pores increases the thermal conductivity in the outer zone

Table 1 Fuel fabrication and operation data for a typical fast-reactor fuel element

|	
Fuel alloy nominal composition (wt%)	U–19Pu–10Zr
^{235}U enrichment (%)	56.99
Fuel slug length (mm)	342.9
Fuel slug radius (mm)	2.16
Fuel slug density (g cm^{-3})	15.8
Fuel smeared density (%)	72.3
Fuel-cladding gap material	Liquid Na
Sodium level above fuel (mm)	6.35
Cladding thickness (mm)	0.381
Fuel-cladding gap width (mm)	0.762
BOL Linear heat rate (W cm^{-1})	420
Subassembly coolant temperatures (°C)	Inlet: 371 Outlet: 486
Subassembly coolant flow rate (l s^{-1})	7
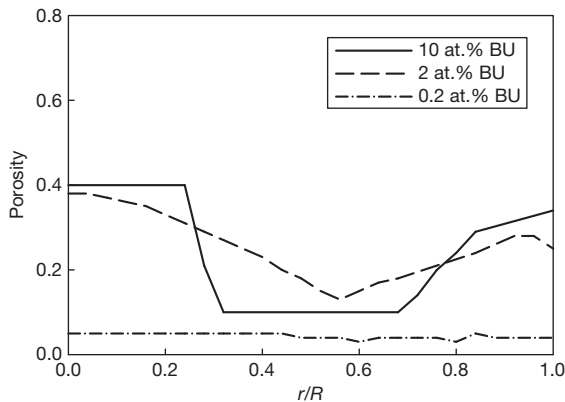
Figure 7 Model predictions of radial porocity distribution in DP-16 (shown in **Figure 4(b)**). Relative radius r/R is a radial position from the center, normalized by the fuel slug radius R.
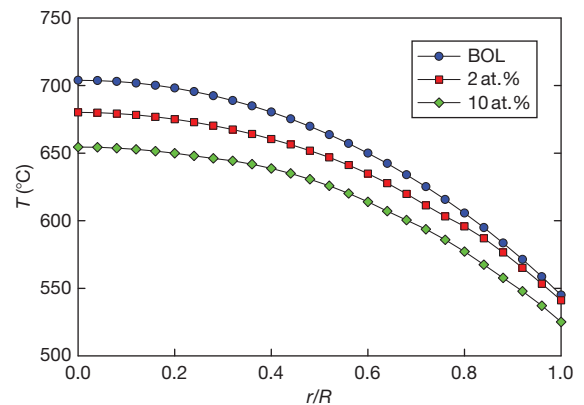

Figure 8 Predictions of radial temperature profile in DP-16. Relative radius r/R is a radial position from the center, normalized by the fuel slug radius R.

restoring the thermal conductivity of the fresh fuel while the dense intermediate zone with the low-Zr concentration also increases the thermal conductivity. The thermal conductivity at the porous center zone decreases about 16%. In general, thermal conductivity gradually changes, so no abrupt changes in temperature profiles occur.

3.23.2.4   Modeling

There are models to predict the phenomenon for U–Zr and U–Pu–Zr alloy fuels. Ogawa and Iwai[18] analyzed the U–Zr system by solving the 1D Fick's equation numerically. A qualitative suggestion regarding the effect of the addition of Pu in U–Zr was made. No experimental data were utilized to verify the model predictions. Hofman et al.[19] analyzed their post-irradiation data to develop a computer model that predicts the redistribution in a binary U–Zr fuel. Model results were parametrically compared with measured U and Zr redistribution profiles to obtain estimates for the necessary kinetic and/or thermokinetic coefficients. Ishida et al.[20] extended a model by Marino[21] for the U–Zr binary system to the U–Pu–Zr ternary system. Assuming that Pu was equally partitioned in U and Zr, they assessed a quasibinary system numerically.

A kinetics model, RECONT,[6] applicable to fuel constituent redistribution in U–Zr or U–Pu–Zr alloy fuels was developed by extending the model used for U–Zr binary alloy fuels. This model was improved later to extend the application range to higher burnup.

RECONT treats U–Pu–Zr as a U–Zr pseudo-binary system by partitioning Pu in U in that Pu migration is relatively small. However, the presence of Pu is indirectly taken into account because it enhances the kinetics of uranium and zirconium migration. U and Zr migrate in directions opposite to each other's.

Since axial temperature gradients are negligible compared to radial gradients and, more importantly, axial constituent redistribution has not been experimentally observed, only radial redistribution is considered. The 1D continuity equation for Zr in cylindrical coordinates is

$$\frac{\partial C_{Zr}}{\partial t} = -\frac{1}{r} \cdot \frac{\partial \left(r \tilde{\mathcal{J}}_{Zr} \right)}{\partial r} + s \qquad [3]$$

where C_{Zr} is the Zr concentration, $\tilde{\mathcal{J}}_{Zr}$ is the interdiffusion flux of Zr, and s is the Zr production rate by fission. The Zr yield per U atom fission is 0.29 and that for Pu atom fission is 0.20.

Within a single-phase field, as was given by Hofman et al.,[19] the Zr interdiffusion flux is given by

$$\tilde{\mathcal{J}}_{Zr} = -\tilde{D}_{Zr}^{eff} \left(\frac{\partial C_{Zr}}{\partial r} + \frac{\tilde{Q}_{Zr} C_{Zr} \partial T}{RT^2 \ \partial r} \right) \qquad [4]$$

where $\tilde{D}_{Zr}^{eff}$ is the effective interdiffusion coefficient of Zr in U–Pu–Zr, $\tilde{Q}_{Zr}$ the heat of transport of Zr in U–Pu–Zr, R the gas constant, and T the temperature. Equation [4], a pseudo-binary equation for the Zr flux, is convenient for use in simplifying the model. This is justified as long as the proper diffusion properties, $\tilde{D}_{Zr}^{eff}$ and $\tilde{Q}_{Zr}$, are provided. With reference to the phase diagram, the single phase occurs only at high temperatures, above ∼650 °C, and the corresponding phase is the γ-phase. Therefore, eqn [4] applies solely to the γ-phase.

Within a dual phase field (strictly speaking, these are pseudo-dual phase fields, such as $(\beta + \zeta) + \gamma$ and $(\alpha + \zeta) + \delta$, the driving force for diffusion is affected by the solubility of Zr in the precipitation phases, $(\beta + \zeta)$ and $(\alpha + \zeta)$, in the present case. This changes the Zr concentration in the continuous phase, given by γ and δ, in the present case. The terminal solubility of Zr in $(\beta + \zeta)$ and $(\alpha + \zeta)$ is described by

$$C_{Zr} = C_{Zr}^0 \exp \left(-\frac{\Delta \overline{H}_s}{RT} \right) \qquad [5]$$

where $\Delta \overline{H}_s$ are the partial molar enthalpies of solution of Zr in the fuel for each phase field. Therefore, the corresponding flux equation in a dual phase field is obtained by substituting eqn [5] into eqn [4] as follows:

$$\tilde{\mathcal{J}}_{Zr} = -\tilde{D}_{Zr}^{eff} C_{Zr} \frac{\Delta \overline{H}_s + \tilde{Q}_{Zr}}{RT^2} \frac{\partial T}{\partial r} \qquad [6]$$

From eqns [4] and [6], it is noticeable that the Zr flux in a single phase is caused by the concentration gradient and the temperature gradient. In a dual phase field, however, only the temperature gradient has a direct effect, whereas the concentration gradient has an indirect effect. Because the temperature gradient is always negative, the sign of $\left(\Delta \overline{H}_s + \tilde{Q}_{Zr} \right)$ determines the direction of the Zr flux. If it is positive, the Zr flux also becomes positive, and the direction of Zr migration is toward the fuel surface; alternatively, a negative Zr flux would indicate Zr migration toward the fuel center.

Casting eqn [3] in finite-difference form gives

$$C_{Zr}^{i,j} = C_{Zr}^{i,j-1} + 2\Delta t \frac{r^{i-1} \tilde{\mathcal{J}}_{Zr}^{i-1,j} - r^{i+1} \tilde{\mathcal{J}}_{Zr}^{i+1,j}}{\left(r^{i+1} \right)^2 - \left(r^{i-1} \right)^2} + \Delta t s^j \quad [7]$$

where Δt is the time-step size, i the ith radial ring and j the jth time-step. Equation [7] is solved using

the flux equations given by eqns [4] and [6]. The time-step size is restricted by the stability criterion

$$\Delta t < \frac{(\Delta r)^2}{2\tilde{D}_{Zr}^{eff}} \quad [8]$$

to generate a valid calculation, where Δr is the radial spatial-step size and $\tilde{D}_{Zr}^{eff}$ is the effective interdiffusion coefficient of Zr. To satisfy this criterion, the computer program divides the time-step further and iterates the whole calculation process internally for the sub-time-steps.

The solution procedure is as follows:

1. The fuel cross-section is divided into radial rings at intervals of Δr.
2. Time is divided while preserving the characteristic time criterion $(\Delta t < \Delta r^2/2\tilde{D}_{Zr}^{eff})$.
3. Fuel temperatures are calculated.
4. The phase field is determined.
5. For a given time interval and for the radial ring, temperature- and concentration-dependent $\tilde{D}_{Zr}^{eff}$, $\Delta\overline{H}_s$, and $\tilde{Q}_{Zr}$ are calculated.
6. $\tilde{\mathcal{J}}_{Zr}$ and direct production s of Zr are calculated.
7. C_{Zr} is updated.

The model prediction of constituent redistribution in DP-16 is compared with measured data in Figure 9. The model prediction has overall consistency with the measured data.

The kinetic parameters that must be known to model the phenomenon are diffusion coefficients, enthalpies of solution of constituents in the second phase in the multiphase fields, and heats of transport of the constituents. However, these data are mostly not available in the literature. Only scarce data for the U–Zr binary fuel are available. A parametric study was done

Figure 9 Comparison of the measured and predicted Zr concentrations in DP-16 irradiated to 11%.

to estimate these data, using the measured data for T179 and DP-16. In this section, a brief summary is given to describe the results.

The effective interdiffusion coefficients $\tilde{D}_{Zr}^{eff}$ for U–Pu–Zr are not available. An iterative method was used to estimate them on the basis of U–Zr binary alloy data available in Hofman et al.[19] The interdiffusivities of the binary system were augmented by an order of magnitude. This enhancement is possibly due to the addition of Pu, rather than the effect of radiation-enhanced diffusion (RED). Since temperatures are relatively high, thermal diffusion effects should be dominant, where thermal annealing of defects generated by fission is effective. Diffusivity change at high burnup is not included in the current model, but will be explored in a future study.

The enthalpies of solution of Zr in the dual phases $(\beta + \zeta) + \gamma$ and $(\alpha + \zeta) + \gamma$ of U–Pu–Zr were estimated by using the Muggianu equation for the Gibbs energy of the ternary solution phases and data for the excess Gibbs free energy of Zr solution in the γ-phase of the U–Pu–Zr alloy, G_{Zr}^E, given as a function of temperature and the Zr content. These data were used to provide the phase diagram shown in Figure 5. The enthalpy of solution can be calculated by the relation

$$\Delta\bar{H}_s = G_{Zr}^E - T\frac{\partial G_{Zr}^E}{\partial T} \quad [9]$$

Heats of transport for the phase regions are simultaneously obtained with other kinetics parameters such as diffusivities and enthalpies of solution. A set of new values have been found to provide reasonable predictions for both lower burnup tests such as T179 and for higher burnup tests such as DP-16.

3.23.2.5 Migration of Minor Actinides and Lanthanide FPs

In a minor-actinide burning reactor such as proposed for the Global Nuclear Energy Partnership (GNEP) system, redistribution of minor actinides (MA = Np, Am, Cm) is of concern because of their potential to react with cladding. The reaction of MA with cladding leads to wall thinning and reduction in cladding melting point. More significantly, MA reactions with cladding will complicate reprocessing, increasing the overall fuel reprocessing costs.

Although metallic fuel irradiations in the EBR-II reactor have generated abundant data, irradiation experience with MA-included metallic fuel is rather limited because the concept of burning MA in fast
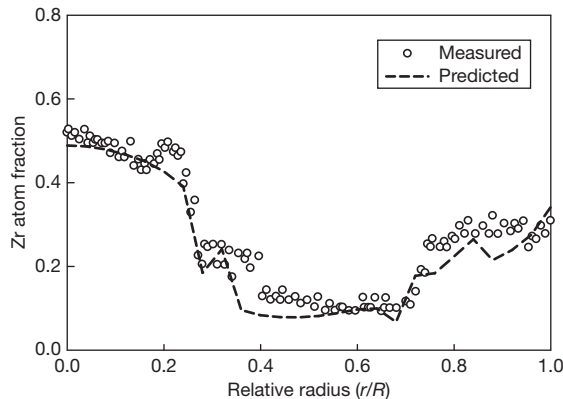
reactors has been introduced only recently. Experiments such as the X501 test from the Integral Fast Reactor (IFR) program have shed some light on this subject.[22,23] The wavelength dispersive spectroscopy (WDS) measurements of G582 fuel element from the EBR-II X501 test are shown in **Figure 10(a)**. The fuel was fabricated by adding 2.1 wt% Am and 1.3 wt% Np in U–20Pu–10Zr and was irradiated to a burnup of ∼6 at.% at the peak fuel centerline and surface temperatures of 700 and 540 °C, respectively. The irradiation achieved 9.1% transmutation of Am. The WDS measurements show typical U, Pu, and Zr redistribution shown in **Figure 3**, and Am is found mainly as precipitates in the regions where large pores were observed. However, Np is more uniformly distributed, much like Pu.
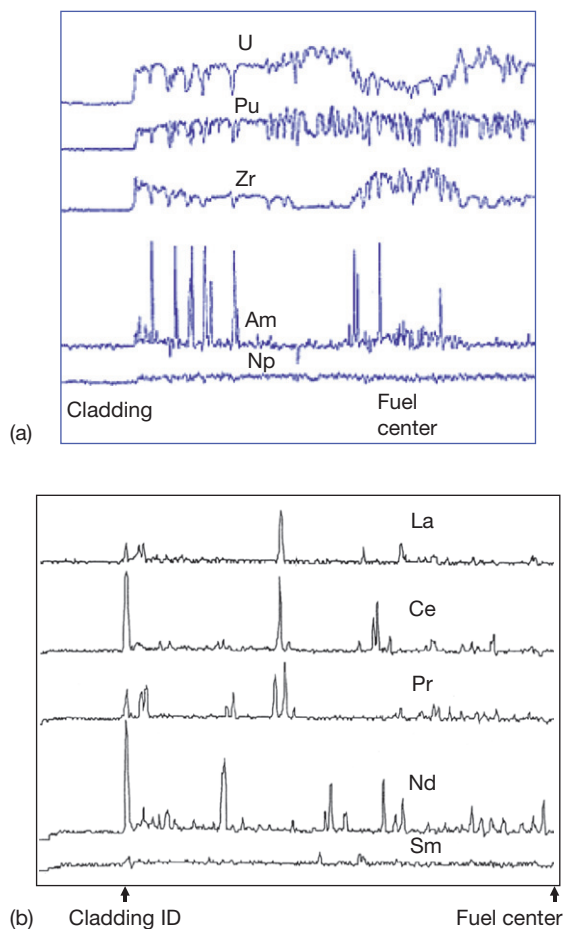

(a)

(b)   Cladding ID   Fuel center

Figure 10 Minor actinide and lanthanide redistribution. (a) U–20.2Pu–9.1Zr–2.1Am–1.3Np (wt%) of G582 from X501 test irradiated to ∼6 at.% burnup. (b) Lanthanide redistribution profiles in irradiated U–10Zr of DP-11 pin in X447 test irradiated in EBR-II to 10 at.% burnup at cladding temperature 650 °C.

In previous models,[22,23] Am migration behavior was explained by a mechanism in which Am vapor moves through interconnected pores down the radial temperature gradient. This mechanism reflects the observation that Am was located mainly where large interconnected pores were available. However, it is also easier for Am atoms to precipitate in the pores than in the fuel matrix because Am has limited solubility in U–Pu–Zr alloy. Furthermore, the vapor transport mechanism cannot explain the observation that Am precipitates are also found in the fuel region where the temperature is higher than in the fuel periphery region. Thus, Am interdiffusion through the fuel matrix and subsequent precipitation in the pores appears to be a more plausible mode. The migration mechanism is probably complex, involving some vapor transport and surface diffusion in interconnected pores in addition to interdiffusion in the fuel alloy.

Lanthanides (LA = La, Ce, Pr, Nd) also accumulate in the fuel, with yields of 0.18 for Nd, 0.17 for Ce, 0.06 for La, and 0.05 for Pr. LA react with stainless steel cladding, and the reaction products lower the cladding melting point. Some of them appear to have migration behavior similar to that of MA. Therefore, test data with LA provide valuable insight into prediction of the behavior of MA-bearing fuel. In particular, considering the high cost and difficulty of dealing with actinides in experiments, the use of surrogate LA seems practical.

The DP-11 fuel element from the X447 test contained U–10Zr and was irradiated in EBR-II to a peak burnup of 10 at.% at the fuel centerline and surface temperatures of 820 and 660 °C, respectively. The fuel temperatures of the DP-11 are ∼100 °C higher than those of G582 shown in **Figure 10(a)**. The DP-11 was tested at a higher-than-typical temperature to obtain a margin in temperature with respect to LA migration and reaction with cladding. The DP-11 is believed to have faster LA migration than more typical, lower temperature tests such as G582. The reaction between LA and the cladding observed in the DP-11 is a direct effect of the high temperature.

As shown in **Figure 10(b)**, the redistribution profiles of LA have large spikes, implying that these peaks are due to precipitates. As given in **Table 2**, most of the lanthanides have limited solubility in U–Pu–Zr, so they precipitate in the fuel matrix. More spikes are seen at the fuel periphery region than the fuel center region, which is similar to the behavior of Am in U–Pu–Zr. The spike strength of Sm is weaker than those of La, Ce, Pr, and Nd because of its lower concentration.

Table 2   Solubility of elements in U–Pu–Zr alloy

Solvent	Solute	Solubility at 600 °C (at.%)	Solvent	Solute	Solubility at 600 °C (at.%)	Solvent	Solute	Solubility at 600 °C (at.%)
	Pu	10		U	24		U	<1
	Zr	<1		Zr	18		Pu	10
	Np	32		Np	16		Np	0
	Am	1		Am	11		Am	NA
U	Cm	NA	Pu	Cm	1	Zr	Cm	NA
	La	0		La	1		La	~0
	Ce	0		Ce	11		Ce	0
	Pr	0		Pr	1		Pr	~0
	Nd	0		Nd	2		Nd	~0

Np and Pu are mutually soluble and both sessile, and show similar migration behavior. Np can be treated as Pu as far as migration is concerned. No test result with Cm is available. Since the yield of Cm is small, the equilibrium concentration of Cm is less than those of Am and Np. Because Cm is chemically more similar to Am and LA, Cm is expected to have a behavior similar to those of Am and LA. Like LA, the solubility of Am in U, Pu, or Zr is very low. Am and LA migration behavior may be generally similar. According to the correlation proposed by Johansson,[24] Am is close to Pr and Nd in chemical and structural properties, suggesting an analogous behavior in migration between these elements.

3.23.3   LIFE-METAL

3.23.3.1   Background

The LIFE-METAL fuel performance code[2,25] has been developed to predict the behavior of metallic fuel rods in fast reactor environment as a function of reactor operating history. The code has evolved from the LIFE series of codes[26] that perform steady-state and design-basis-transient analyses for the thermal, mechanical, and irradiation behavior of nuclear fuel rods. The original code was developed for UO_2 and mixed oxide fuels for use in fast reactor systems, where LIFE-4 Rev. 1 is the latest oxide fuel version of the code.[27] Another version of the code is LIFE-4CN,[28] which was the basis for LIFE-METAL and included two fuel options, ((U, Pu)C and (U, Pu)N). All code versions include detailed thermomechanical analysis that is performed in the radial direction with provisions to specify up to 20 radial rings for the fuel–cladding system as shown in **Figure 11**, where different rings are used for thermal and mechanical
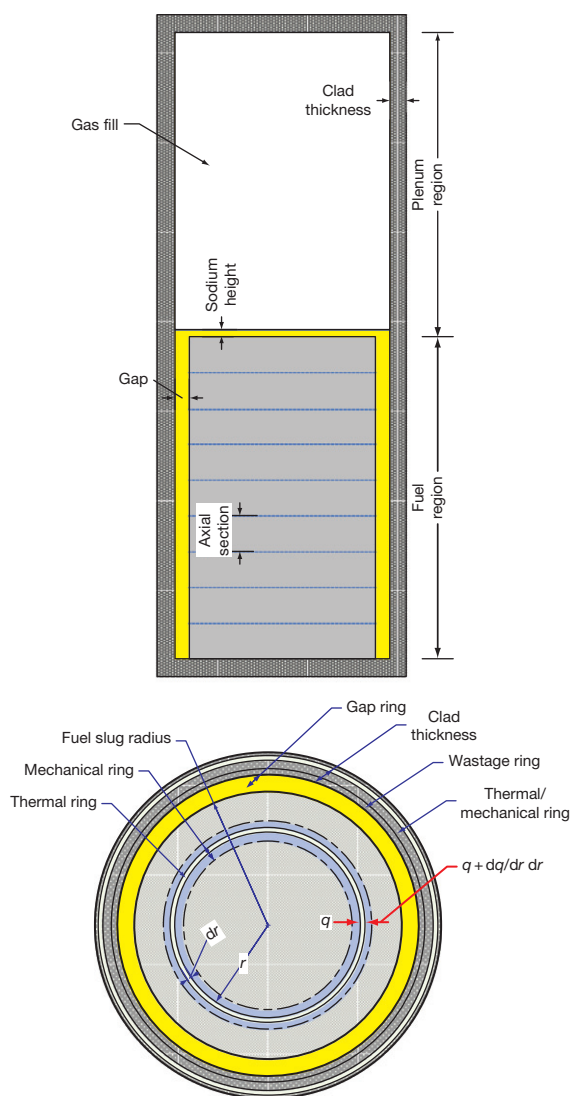

Figure 11   Fuel pin axial and radial representation in the LIFE code.

analysis. Axial variations in operating conditions are accounted for by using powers and fast fluxes for up to nine fuel axial nodes and one plenum node. Thermally, the axial nodes are coupled through the calculated coolant temperatures. Axial heat conduction is ignored and there are no provisions for mechanical coupling between axial nodes. A detailed mechanical analysis is performed for both fuel and cladding, utilizing the generalized-plane-strain assumption for each axial segment and incorporating a large strain capability. The solution procedure involves iteration on local total strain within each time step, and the solution procedure is explicit in time.

LIFE-METAL code development has been associated with the IFR program,[29] where the code was the focus of the program activities related to prediction of fuel-pin behavior under normal operating conditions. Predictions of interest about the nuclear design are changes in fuel length and fissile content due to burnup and breeding. Thermal predictions about fuel temperature, design margins to fuel melting, and design margins to low-melting-temperature alloy (e.g., U–Fe) formation are also of interest. Mechanical predictions useful to designers are FCMI and FCCI, cladding deformation and design margin to significant coolant flow area reduction, and cladding damage and design margin to cladding failure due to fission gas pressure loading.

The code has been extensively used for planning steady state and transient experiments at EBR-II, given the initial conditions for transient fuel performance codes such as FPIN code[30] in addition to performance evaluation of new fuel designs and out-of-pile experiments.[31,32] For example, the code was used to evaluate the expected performance of EBR-II Mk-V fuel design[25,33] and was used to check the performance against prespecified design criteria. LIFE-METAL code development was frozen in 1994 with the termination of the IFR program. Recently, Toshiba Corporation and Central Research Institute of Electric Power Industry (CRIEPI) has initiated the preapplication review of its Super Safe, Small, and Simple (4S) fast reactor in the United States, through informing the United States Nuclear Regulatory Commission (NRC) on the reactor's systems and fuel design. The code has been used in relation to this activity where evaluation of 4S reactor fuel design[34] was performed. In addition, recent developments in the US fast reactors program have brought back interest in the code as a metallic fuels code that can be used for verification and validation of future detailed 3D finite element code to be developed as

part of the Fuel Cycle Research and Development (FCR&D) modeling and simulation effort. This interest is a motivation for a future activity for improving the code models to accommodate possible advanced designs that include MA and possibly achieve higher burnups.

The following sections describe general code differences from previous versions, including a brief description of specific models that are associated with significant metallic fuel performance characteristics and their treatment in the code. Discussion of code validation and possible future developments are also presented.

3.23.3.2   Code Structure and Models

This section briefly describes the general code structure and key models of interest to metallic fuel behavior.

3.23.3.2.1   Code structure and thermomechanical analysis

As mentioned before, the original version of the LIFE code[26] was aimed at simulation of oxide fuel behavior. Later code versions, including LIFE-METAL, maintained the same general structure of the oxide code with different materials properties included and specific models being added or removed, according to the type of fuel. Detailed description of the code structure is presented elsewhere.[26,35]

In converting LIFE-4CN to LIFE-METAL, a number of fuel properties and models were changed and/or added. Fuel property correlations for U–5Fs and U–xPu–yZr were first developed as continuous functions of temperature, porosity, alloy composition, stress, fission rate, burnup, etc. Here, Fs stands for fissium, a mixture of metals: 2.46Mo, 1.96Ru, 0.28Rh, 0.19Pd, 0.1Zr, and 0.01Nb (in wt.%), which is the equilibrium composition of residual materials left in the melt-refining process (see **Chapter 3.01, Metal Fuel**). The physical and thermal properties include density, phase-change temperatures, specific heat, thermal expansion, thermal conductivity, and alloy and FP distributions. The mechanical properties include elastic moduli, fracture strength, and thermal and fission-enhanced creep.

Physical, thermal, mechanical, and irradiation property correlations for test and design cladding materials (e.g., austenitic 316, austenitic D9, and ferritic HT9) are included in the code. Some work has been done during LIFE-METAL development to improve the correlations (e.g., D9 creep and swelling)

in order to get a better fit to the database within the operating range of interest for metallic fuels. Wastage correlations for sodium–cladding interaction and time and strain-failure correlations are also included. Models were developed for Ni depletion from D9 cladding and carbon depletion from HT9 cladding due to the FCCI. Empirical eutectic penetration correlations, based upon fuel behavior test apparatus (FBTA)[36] and whole-pin-furnace (WPF)[32] test data, are also incorporated.

In order to extend the LIFE code to simulation of metallic fuel, in addition to changes in the basic fuel properties, a number of models were removed or became no longer important in the metallic fuel version. Those phenomena include fuel restructuring and hole formation, crack formation and healing, oxygen and porosity migration, hot pressing and sintering, and gap conductance. Other phenomena such as FCCI, fission gas driven swelling and gas release, migration of fuel constituents, transport of FPs, and fuel thermal and irradiation creep remained important. However, approach to each of those phenomena is different between oxide and metallic versions of the code. Of those phenomena, the important metallic fuel (U–Zr and U–Pu–Zr) issues encountered in previous US designs are related to FCCI, fuel constituent redistribution and swelling, and fission gas release.[1,37] Those phenomena impact cladding degradation and fuel swelling rates during operations. The following subsections briefly discuss each of these issues and its implementation in the LIFE-METAL code.

3.23.3.2.2 Constituent redistribution

Constituent redistribution in a metallic U–Pu–Zr alloy fuel under fast reactors operating conditions is a commonly observed irradiation phenomenon as discussed in detail in **Section 3.23.2**. There are a number of performance degrading issues associated with this phenomenon. The reduction of Zr fraction in regions within fuel reduces their melting points and potentially reduces power to melt during accident sequences. However, this effect of Zr reduction can be limited as follows. During normal operations of a metallic fuel type fast reactor, temperature drop across fuel is small (usually <100 °C). This is as a result of metallic fuel high thermal conductivity and negligible temperature drop across the fuel–cladding gap due to the presence of sodium bond. As a consequence, peak fuel temperature is dictated by the limit on inner clad temperature, which is dependent on the type of cladding. For example, the HT9 ferretic–martensitic steel has limited

thermal creep properties which impose a nominal inner clad temperature that is <620 °C. This leads to peak fuel temperatures that are far from the melting temperature even in regions where Zr is depleted, though Zr reduction lowers the margin for fuel melting during a transient.

A more significant effect of redistribution is its impact on fuel swelling rates and axial fuel growth. The multiple radial zones present across fuel radius as shown in **Figure 4**, due to the redistribution phenomenon, have different growth rates, and are believed to play a role in observed metallic fuel anisotropic growth.[1] This anisotropic fuel growth, in which axial growth rate is lower than radial growth rate, was observed in U–Zr-based fuel (anisotropy increases with increasing Pu content as shown in **Figure 12**) and where constituent redistribution takes place. Another indirect effect of the redistribution phenomenon is its possible relation to the fuel–cladding gap closure time, in which varying redistribution levels and associated differences in radial swelling can axially vary the time for gap closure. Kim et al.[38] describe associated lock-up effects and the impact on fuel axial growth, in which the part below the spot in which the gap closure occurs stops to contribute to axial growth. This variation in gap closure time is shown in **Figure 13**.

Axial fuel growth estimates in the original LIFE code are based on the assumption of isotropic fuel growth during irradiation. LIFE-METAL adds the effects of anisotropic growth using a simple linear growth model as follows. The axial swelling behavior
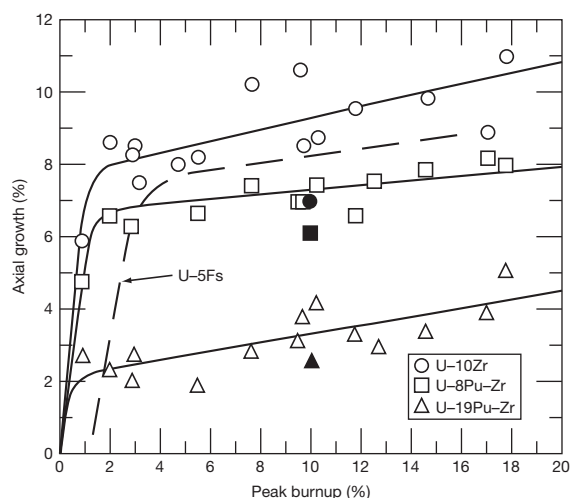

Figure 12 Fuel length increase in various metallic fuels as a function of burnup. (Closed symbols correspond to the IFR-1 data.)
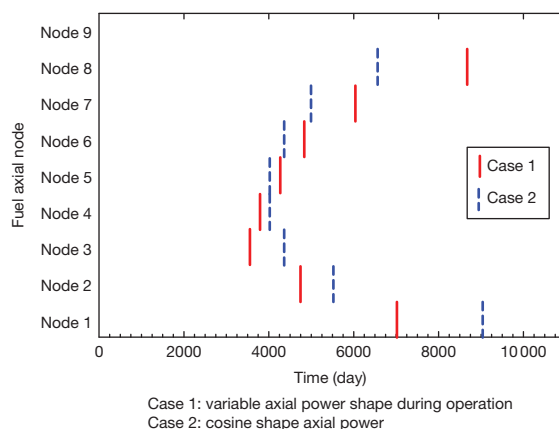
Figure 13 Predicted time for the fuel–cladding gap closure for low-power (40 W cm^{-1}) fuel pins by the lock-up model. Reproduced from Kim, Y. S.; Yacout, A. M.; Hofman, G. L.; Ryu, H. J. *Trans. Am. Nucl. Soc.* **2007**, *96*, 709.

is caused by fuel swelling over the initial 1.0–1.5 at.% burnup range. Beyond that burnup, fuel is assumed to be in contact with cladding and additional axial growth progresses at a much lower rate. The axial growth is described by the following equations:

$$\text{For } Bu \leq 0.75 \text{ at.\%}, \Delta L/L_{o}(\%) = m_1 Bu \quad [10]$$

$$\text{For } Bu > 0.75 \text{ at.\%}, \Delta L/L_{o}(\%)$$
$$= 2.75 + m_2(Bu - 0.75) \quad [11]$$

where m_1 and m_2 are calibration constants, and in each case Bu is the peak burnup in the fuel element (at.%). Figure 14 shows a comparison of LIFE-METAL predictions of fuel axial expansion and measured data for U–Zr–Pu fuel. Note that the existing database for axial fuel growth shows considerable scatter, as shown in the figure, which can be explained largely by the scatter in the fuel operating temperatures.

A more rigorous treatment of the redistribution phenomenon is given in **Section 3.23.2**, where the time and temperature dependence of concentration of redistributed elements and associated impact on fuel swelling are considered. Future plans for the LIFE-METAL code include implementation of those models and tying it to fuel swelling, improving the mechanistic aspect of the code.

3.23.3.2.3 *Fuel–cladding chemical interaction*
An example of FCCI, as shown in **Figure 15**, where interdiffusion between metallic U–10Zr fuel and cladding components takes place, represents a twofold potential problem for metallic fuel. It both weakens the cladding mechanical properties and leads to the
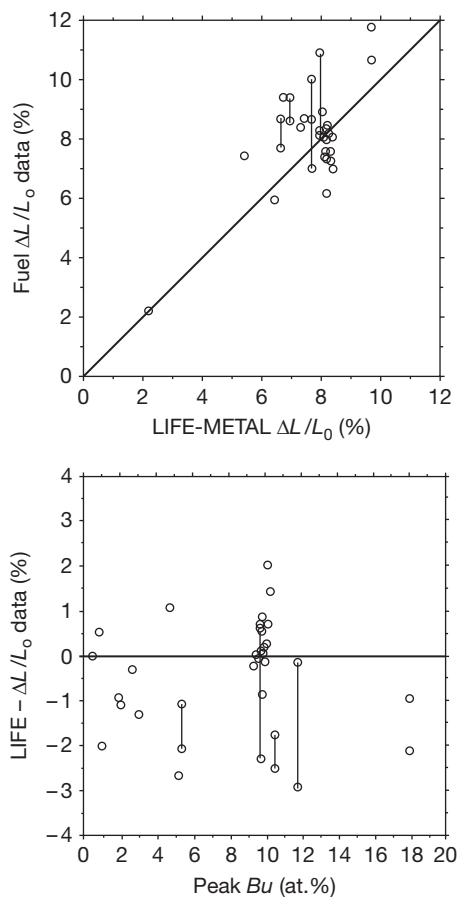

Figure 14 Predictions versus axial expansion ($\Delta L/L_{o}$) data for U–xPu–10Zr fuel.

formation of compounds having relatively low melting points in both fuel and cladding. During normal operations, FCCI is characterized by solid-state interdiffusion although liquid phase formation might be expanded during transients reaching 700–800 °C.

In general, FCCI in metallic fuel can be characterized by two stages of interaction as shown in **Figure 16**, where the different possible cladding wastage mechanisms are indicated.[39] Prior to accumulation of lanthanide FPs at the fuel–cladding interface (due to FPs migration), FCCI is characterized by a ferretic layer formation. This layer can be a result of Ni depletion in austenitic cladding or decarburization of the martensitic cladding. This type of interaction has solid-state diffusion type time and temperature dependence.

Ultimately, rare-earth FPs (lanthanides) control FCCI as they migrate to the fuel–cladding interface in amounts that are functions of both burnup and extent of radial migration in fuel (see **Section 3.23.2** for more details on lanthanides migration in metallic
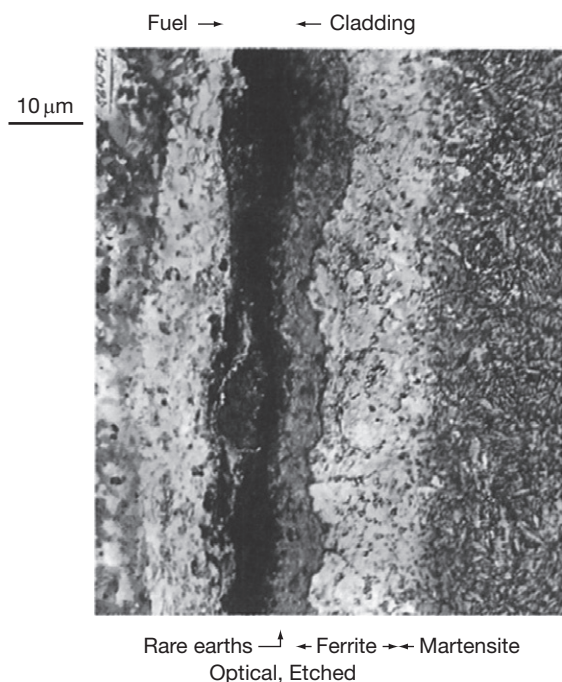
Fuel →   ← Cladding

10 μm

Rare earths ⤴ ← Ferrite →← Martensite
Optical, Etched

Figure 15 Interdiffusion between U–10Zr fuel and HT9 cladding irradiated to 6 at.% burnup at ~620 °C.

fuel). This radial migration increases with both fuel temperature and presence of Pu in the fuel. Modeling of FCCI and FP migration should be accompanied by better understanding of the possible complex phase relations between cladding and fuel constituents and some of the FPs. Efforts to experimentally establish those phase relations were started at Argonne National Laboratory in the early 1990s as part of the IFR program.[40] The effort continued in Japan[14,41] after the termination of the IFR program. However, much remains unfinished in this area of predicting the phase relations to match the experiments, which can now be complemented with extensive advanced phase diagram simulations.[42] In addition to the understanding of the FCCI phenomena, efforts are currently directed toward different possibilities to reduce its effect on cladding performance. These include the use of a barrier of zirconium, vanadium, or zirconium-nitride on the cladding inner surface. Another possibility is to investigate fuel alloy additions to slow down or impede diffusion of certain FPs that are important to FCCI[43] as discussed in **Section 3.23.2**.

Empirical diffusion-type models that account for FCCI have been implemented in the LIFE-METAL

Scratches on outer diameter

C/Ni depleted zone on outer diameter

C/Ni depleted zone on inner diameter

Lanthanide-rich zone
Eutectic liquefaction

Scratches on inner diameter

Original cladding Inner diameter

Load bearing Ligament

Original cladding Outer diameter

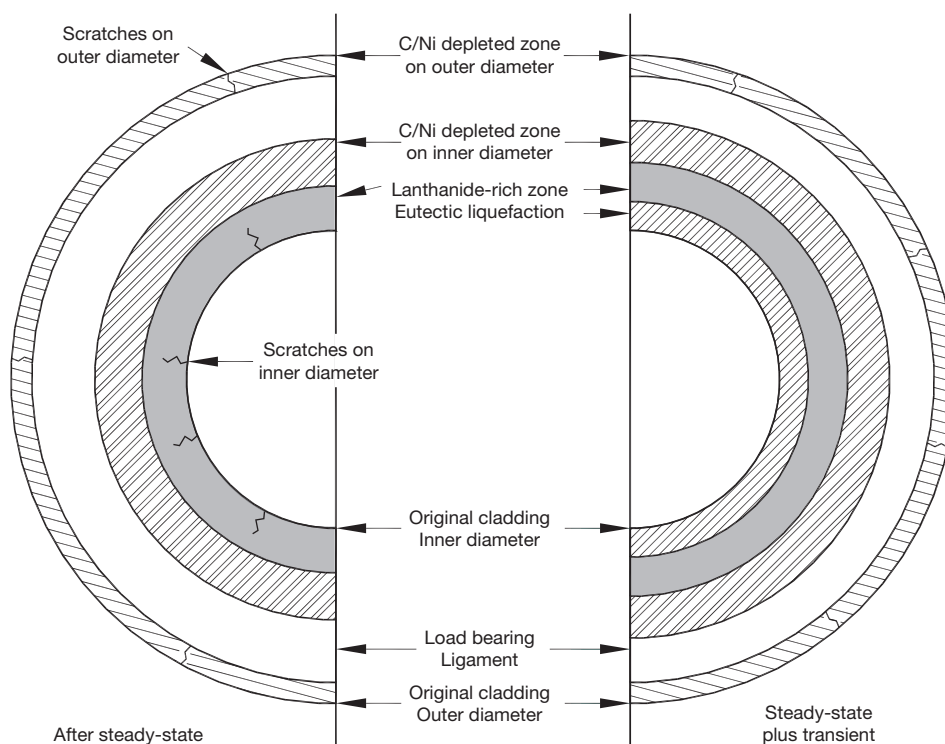After steady-state

Steady-state plus transient

Figure 16 Cladding wastage mechanisms. Reproduced from ANL-IFR-244. Integral Fast Reactor Program Annual Progress Reports FY 1993, Oct 1994.
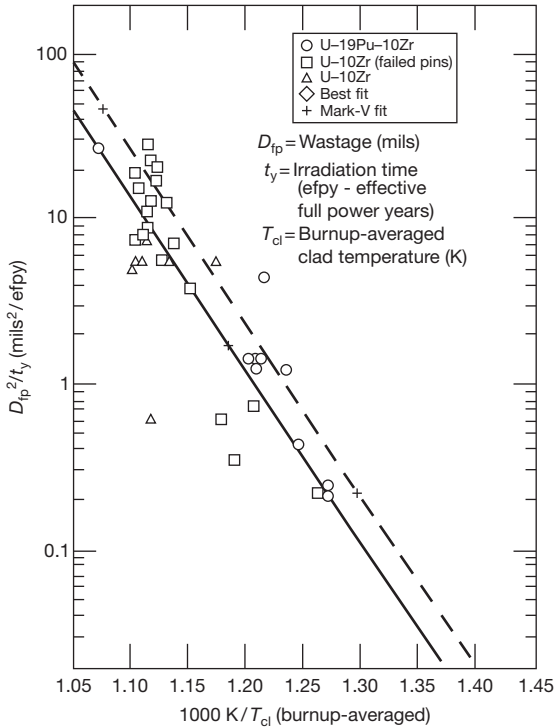
Figure 17 Steady state wastage correlation for HT9 clad fuel. Reproduced from ANL-IFR-244. Integral Fast Reactor Program Annual Progress Reports FY 1993, Oct 1994.

code. The correlations used are based on cladding wastage data from fuel irradiated at EBR-II as shown in **Figure 17**.[25] The figure compares the code's estimates with the wastage data.

LIFE-METAL has provisions to take wastage into account[44] based on the different wastage mechanisms shown in **Figure 16**. The cladding thickness is reduced from its nominal value due to inner-diameter (ID) and outer-diameter (OD) fabrication tolerances and scratches; due to OD sodium–cladding corrosion, decarburization, and intergranular attack; and due to ID fuel–cladding chemical or metallurgical interaction (FCCI). For both, HT9 and 316SS claddings, ID FCCI is characterized by FP diffusion into the cladding and some cladding constituent (e.g., Fe, Ni, Cr, C, etc.) diffusion to the fuel.[1] The FP-rich cladding layer tends to be very brittle, that is, high in microhardness, and easy to be cracked, so it is not reliable as a load-bearing layer. LIFE-METAL assumes δ_o and δ_i as cladding thicknesses to be removed from the cladding OD and ID, respectively, for the purposes of the structural analysis. This is reasonable in that it is assumed that the dominant contribution to δ_o is corrosion. In the case of ID corrosion, δ_i defines a cladding layer thickness that is present for both, the thermal

analysis and for determining fuel–cladding gap closure. However, the shear modulus is reduced by a factor of 10 and the creep rate of this layer is increased by a factor of 100 to make this FP-rich layer essentially non-load-bearing. It simply transmits the gas pressure or FCMI interface stress unabated to the intact base cladding.

In LIFE-METAL, it is recommend that a tolerance/scratch allowance of 1.27×10^{-2} mm (0.5 mils) be used for both the cladding ID and OD. Also, given the fact that temperature and operating conditions change with time, it is recommended that δ_o and δ_i be determined from rate laws:

$$\delta_o(\text{mm}) = 1.27 \times 10^{-2} + 2.54 \times 10^{-2} \int_0^t \dot{\delta}_o \mathrm{d}t \quad [12]$$

and

$$\delta_i(\text{mm}) = 1.27 \times 10^{-2} + 2.54 \times 10^{-2} \int_0^t \dot{\delta}_i \mathrm{d}t \quad [13]$$

The $\dot{\delta}_o$ functional form and parameters[44] are determined from the cladding properties and the type of fuel. The rate correlations for clad ID corrosion are based on steady-state irradiation results and post irradiation FBTA and WPF test results. The D9/U–19Pu–10Zr and HT9/U–19Pu–10Zr database is used as a guide in modeling the D9 and HT9 cladding fuels as shown in **Figure 17**. For temperatures ≤ 650 °C, the correlation for $\dot{\delta}_i$ is given by a typical diffusion layer growth equation as follows[44]:

$$\dot{\delta}_i = 1.27 \times 10^{-2} [D_o \exp\left(-Q/RT_{ci}\right) + D_{io}\phi]^{0.5} t^{-0.5}$$
$$[14]$$

where ϕ is the neutron fast flux in 10^{15} n cm^{-2} s; R, 4.18 J mol^{-1} K; Q is the activation energy in J mol^{-1}; T_{ci}, cladding ID temperature in K; $\dot{\delta}_i$, wastage rate in mm h^{-1}; and t is the time in s. Correlation constants, D_o, Q, and D_{io}, depend on the type of cladding and fuel combination.

3.23.3.2.4   Fuel swelling and fission gas release

Swelling behavior of metallic fuel alloys is well documented.[1,45] The general swelling behavior of those alloys is illustrated in **Figure 12** by an increase in fuel length versus burnup. As shown in the figure, swelling proceeds rather rapidly with burnup at burnups smaller than ~1 at.%, which is one of the characteristics of metallic fuel behavior. Virtually all length increases take place during that burnup interval

before the fuel slug comes into contact with the cladding. The leveling-off in length increase is thus determined by the fuel smeared density. As mentioned before, the behavior shown in the figure is an anisotropic behavior in which the axial growth proceeds more slowly than the radial growth, and the extent of anisotropy increases with increasing the fuel's Pu content. This axial growth behavior is represented in the LIFE-METAL code by a correlation and no mechanistic model is implemented. Recently, a model that combines the predictions of constituent redistribution with axial lock-up effects was used to predict metallic fuel axial growth.[38] However, this model still uses fixed axial growth rates that are dependent on burnup, as the two distinct axial growth regimes shown in **Figure 12** are represented by two fixed growth rates.

Although kinetic fission gas release models (such as a model by Rest[7]; also see **Chapter 3.20, Modeling of Fission-Gas-Induced Swelling of Nuclear Fuels**) are available, none has been implemented in the LIFE-METAL code. Instead, fission gas release fractions are calculated by a phenomenological correlation. Future activities in this area will attempt to implement a mechanistic fission gas release model into the code. In addition, a more detailed modeling of fission gas release considering fuel microstructure evolution is subject of future activities.

A summary of LIFE-METAL implementation of an empirical fission gas release model is given by Billone et al.[2] In this model, the rate of increase of retained fission gas in a fuel ring, $\dot{G}_s$, is found by a simple balance between the rate of gas production, $\dot{G}_p$, and the rate of gas release,

$$\dot{G}_r = F_g G_s \quad [15]$$

$$\dot{G}_s = \dot{G}_p - F_g G_s \quad [16]$$

The fractional gas release rate F_g (s^{-1}) is given as follows:

$$F_g = \left[1 - e^{-\alpha \cdot Bu}\right]\left[1 + c_g(P - 0.1)^{-2/3}\right]$$
$$R_g e^{(-Q_g/RT)} + f(\varepsilon_s - \varepsilon_{si}) \quad [17]$$

where Bu is burnup in at.%, P is porosity ($0.1 \leq P$), T is the temperature in K, and ε_s is the fuel swelling strain $0 \leq (\varepsilon_s - \varepsilon_{si})$. α, c_g, R_g, Q_g, f and ε_{si} are empirical parameters to be determined from in-reactor data. For $0.3 \leq \varepsilon_{si}$, the second term is orders of magnitude larger than the first term, giving rapid gas release when fuel swelling of gas bubbles becomes >30%.

The LIFE-METAL fuel-swelling model includes incompressible and compressible FP swelling. The latter part is due to gas bubble growth. The strain by compressible FP swelling is calculated from a model that assumes a number density c_b of bubble nucleation sites, which is independent of burnup but dependent on temperature according to

$$c_b = B_b e^{(Q_b/RT)} \quad [18]$$

where c_b is in cm^{-3}, B_b and Q_b are empirical constants. The model also includes a nonequilibrium effect by allowing bubbles to grow to their equilibrium size at a rate proportional to the creep rate. Thus, more bubble nucleation sites are predicted to exist at lower temperatures, and the fewer gas atoms per bubble (along with the reduced rate toward equilibrium) will result in smaller bubbles and less swelling strain.

As experimental data for U–Zr and U–Pu–Zr fuel became available, the different sets of LIFE-METAL calibration constants were derived. **Figure 18** shows LIFE-METAL predicted and measured fission gas release in U–10Zr. Similar comparisons have been made for U–Pu–Zr fuel data.

3.23.3.3 LIFE-METAL Validation

The following validation discussion is based on the last code validation activities performed by Billone.[44] This validation effort has been extensive as it used post irradiation examination (PIE) data that are available from a large number of metallic fuel-pin irradiations at EBR-II and FFTF.[46] PIE data include fission gas release, fuel volumetric and fuel length change, cladding diametral change, and cladding wastage. Axial profiles are available for fuel radial growth at low burnup (prior to and including initial fuel–cladding contact) and for cladding radial growth for a wide range of burnups and fast fluences. Some data that are available on a more limited basis are radial and axial variations in U, Pu, Zr, fission gas porosity, axial variations in fraction of porosity filled (logged) with Na, and depth of C-depleted and Ni-depleted zones in HT9 and D9, respectively. Fairly complete sets of data are available for 80 fuel-pin irradiations (111 pins in total were used in the validation). Limited data (e.g., fuel length change, cladding diameter change) are available for hundreds of irradiated fuel pins.

The validation database includes three cladding types (cold-worked, austenitic D9 and 316 stainless steels and HT9 ferritic–martensitic steel) and eight fuel compositions (U–10Zr, U–3Pu–10Zr, U–8Pu–10Zr, U–19Pu–6Zr, U–19Pu–10Zr, U–19Pu–14Zr, U–22Pu–10Zr, and U–26Pu–10Zr, where the numbers represent weight percents). The data from the 111 pin irradiations fall into one or more of the following categories: fission gas release (FGR), fuel
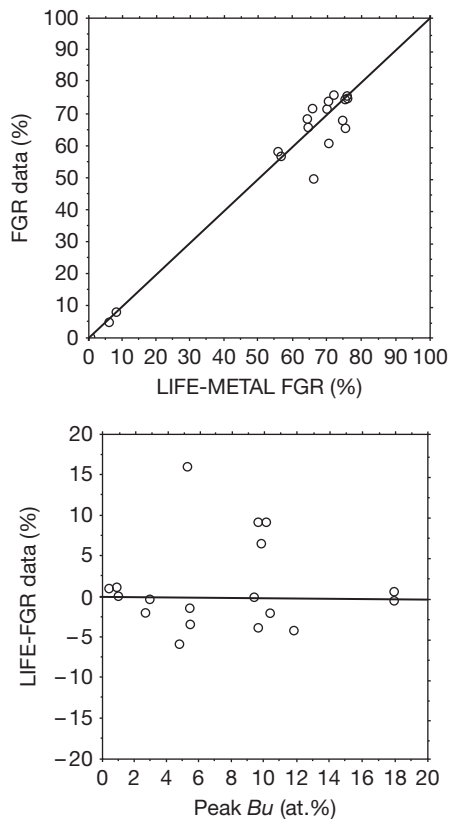
Figure 18 Predictions versus fission–gas–release (FGR) data for U–10Zr fuel.

axial strain ($\Delta L/L_o$), fuel diametral strain ($\Delta D/D_{of}$), cladding diametral strain ($\Delta D/D_o$), and penetration depth (wastage) at the cladding inner diameter (ID) due to ingress of FP and egress of cladding constituents. For the last three categories, axial profiles are often available. This implies a large number of data points per fuel element irradiation. Also, in the case of fuel axial expansion and peak cladding strains, which are routinely measured for all elements within a subassembly, the number of data points is much larger than the number of validation cases. Table 3 summarizes the number of fuel–cladding combinations for the validation dataset, as well as the number of data points for each category.[44] The '+' superscript next to a number indicates that more data are available from sibling elements within a subassembly than used directly in the validation effort.

An example of a validation dataset is the HT9 dataset from EBR-II experiment X441.[47] This experiment was designed to provide benchmark data for the LIFE-METAL code. This dataset has a peak cladding temperature (600 °C) and a peak linear heat rate (52.5 kW m^{-1}). The reference X441 pins had typical EBR-II fuel and cladding dimensions such as those shown in Table 1. The design variables for X441 are Zr content (6–14 wt%), plenum-to-fuel volume ratio (1.0–2.1), and fuel smeared density (70–85%). Code predictions were compared with experimental data

Table 3 Summary of fabrication, operating conditions, and PIE data for LIFE-METAL validation

| Fuel type | Cladding type | Burnup range (at.%) | PICT (°C) | Number of PIE data points | | | | |
| | | | | FGR | Wastage | $(\Delta L/L_o)$ | $(\Delta D/D_o)$ | |
							Peak	Profile
U–10Zr	D9	0.8–18.0	535–620	10	14	13+	6+	5+
	316SS	0.5–5.0	500	3		4+	1+	0+
	HT9	2.8–18.5	530–660	4	30	19+	19+	7+
U–3 Pu–10Zr	316SS	0.5–5.0	500	4		4+	1+	0+
U–8 Pu–10Zr	D9	0.8–18.0	535–565	10		11+	5+	5+
	316SS	0.5–5.0	500	4		4+	0+	0+
	HT9	2.8–16.0	530	1		3+	1+	1+
U–19 Pu–10Zr	D9	0.8–18.0	535–590	12	21	14+	9+	9+
	316SS	0.5–5.0	500	4	6	4+	2+	0+
	HT9	2.8–19.5	530–590	8	9	9+	17+	10+
U–19 Pu–6 Zr	HT9	5.0–10.0	575	2		1+	2+	1+
U–19 Pu–14Zr	HT9	6.0–13.0	590	2		2+	2+	1+
U–22 Pu–10Zr	316SS	0.5–5.0	500	4		4+	1+	0+
U–26 Pu–10Zr	316SS	0.5–5.0	500	3		4+	1+	0+
	HT9	2.2	534	1		0+		
Data total				*72*	*80*	*92+*	*68+*	*51+*

PICT is peak inner cladding temperature, FGR is fission gas release, $(\Delta L/L_o)_f$ is fuel axial strain, and $(\Delta D/D_o)_c$ is cladding diametral strain.

for cladding strain, fuel length change, and fission gas release. This specific experiment was a vehicle for validating the FCMI model in LIFE-METAL. Figure 19[25] shows the predictions (lines) versus data (points) as a function of smeared density for two different exposures (0.59 full power years and 1.25 full power years). As shown in the figure, the agreement is good for all of the low-burnup data, while high-burnup strain data were overpredicted in the 85% smeared density elements. Other experiments that were designed to benchmark LIFE-METAL for estimating the behavior of blanket fuel pins are experiments X431 and X432.[47] Different comparisons between LIFE-METAL estimates and experimental data are shown in Figures 20 and 21. Figure 20 shows good agreement between the LIFE-METAL predictions and the data for the peak HT9 and D9 cladding strains for 75% smeared density U–19Pu–10Zr pins.[44] The difference between LIFE predictions and data is generally within the uncertainty and pin-to-pin scatter (about 0.087%). Figure 21 shows specific detailed pin validation of LIFE-METAL calculations to pins data from EBR-II experiment X425. Finally, accompanied with this code validation effort, there were efforts to improve the associated database by improving the estimates of the operating parameters associated with the experimental data, especially since IFR program utilization of EBR-II relied in large part on calculations of operating parameters.[48–51] The improvements in EBR-II operating parameters database were based on generating consistent data for each subassembly on the
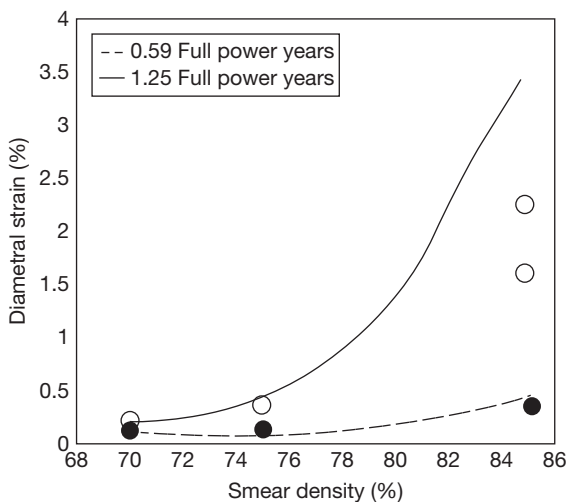
basis of detailed neutronics and thermal hydraulics calculations to provide the parameters for each irradiated pin at any axial location.
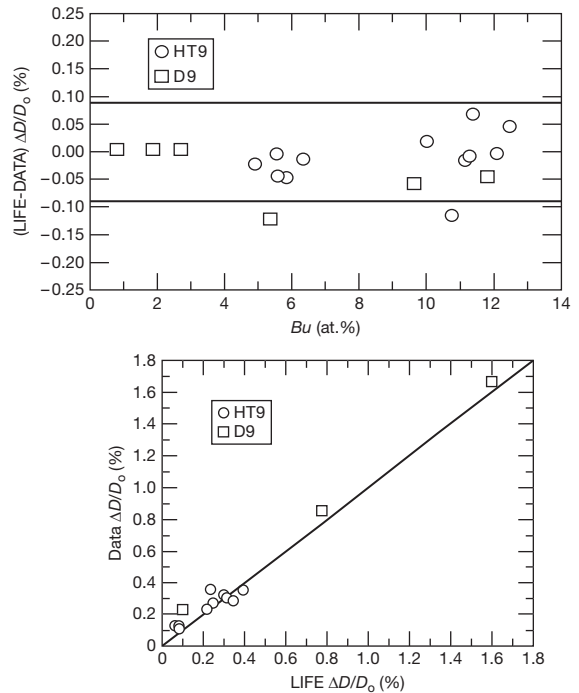
Figure 20 LIFE-METAL versus data for U–19Pu–10Zr/HT9 cladding strain.

Figure 19 Measured and predicted peak cladding diametral strain in X441 elements as a function of smeared density and exposure time.
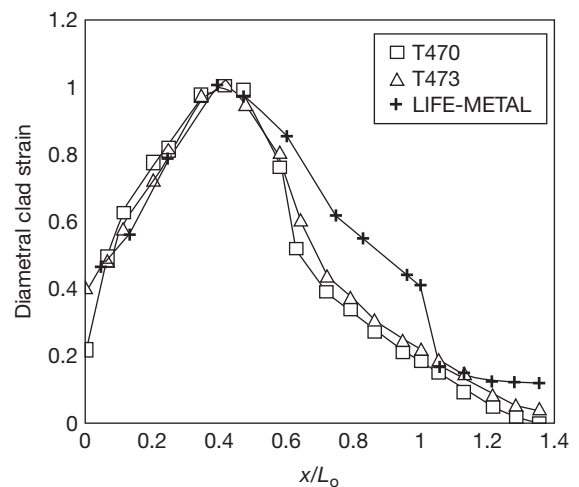

Figure 21 Measured and LIFE-METAL predicted diametral cladding strain profile for X425 experiments. Reproduced from ANL-IFR-169. Integral Fast Reactor Program Annual Progress Reports FY 1991, June 1992.

3.23.3.4 LIFE-METAL Code Status and Future Activities

The latest calibration of the LIFE-METAL code was performed just before the termination of the IFR project in 1994. Sets of verification test problems that correspond to data from different EBR-II experiments are available and have been used systematically to verify the code calculations.

Minor changes have been done to the code since its calibration. Those changes did not affect the code's calibration and were mainly aimed at correcting a code error associated with FCCI for fuels with long irradiation periods.

As for future plans for improving the code, modeling effort will be required to reevaluate the effect of constituent redistribution, FP migration, and fission gas release, and improve LIFE-METAL's existing models by including mechanistic models to account for the synergistic effects of those phenomena.[6,7] Those code improvements can provide better predictions about fuel swelling and fuel thermal behavior, including fuel thermal conductivity. New models for FCCI will need to be developed focusing initially on rare-earth FP diffusion and their interactions with cladding; and phase diagrams for alloys of rare earth and cladding constituents are needed.

Metallic fuel remains to be a candidate for use as a transmutation fuel containing minor actinide elements such as Am and Np in addition to U, Pu, and Zr.[52] Inclusion of models for the behavior of MA in the LIFE-METAL code will be a high-priority task for the future code development, which is dependent on the availability of experimental data and a better knowledge of phase diagrams for those elements with other fuel components.

3.23.4 ALFUS

3.23.4.1 Background

For a comprehensive understanding of the mechanical behavior of metal fuel during irradiation, the computer code ALloyed Fuel Unified Simulator (ALFUS)[3,53] was developed. The ALFUS code includes the following analytical models:

1. a stress–strain analysis model, including gas bubble compressibility and open pore volume decrease,
2. a mechanistic model to describe coalescence and growth of the gas bubbles, formation of the open pores, and fission gas release,

3. an empirical model to incorporate the effect of large radial crack formed in the U–Pu–Zr ternary fuel slug,
4. a model to calculate the volume increase of the fuel alloy matrix due to accumulation of nongaseous FPs (solid FP swelling),
5. an empirical correlation to estimate the cladding wastage by rare-earth FP,
6. a temperature analysis model with effective thermal conductivity of the porous slug infiltrated by the bond sodium.

These models are linked in ALFUS so that the relations among in-reactor phenomena in metal fuel pins can be simulated properly. Input data for ALFUS are fuel pin specification and irradiation condition, such as linear power rate and its axial distribution, coolant flow rate per pin, and coolant inlet temperature. A set of model parameters, the physical and mechanical properties of the fuel alloy and cladding, is also required. The ALFUS code outputs temperature distribution and stress–strain state in the slug and cladding, fission gas release, margin to cladding creep rapture (cumulative damage function, CDF), etc.

Changes in the melting temperature (solidus and liquidus) of the fuel slug due to the fuel constituent migration are important when the design limit of the fuel pin is evaluated, so ALFUS includes the thermo-diffusion model[20] to simulate the fuel constituent migration. However, this model is not used since the stress–strain calculation in the current version of ALFUS is relatively insensitive to changes in the local compositions of the fuel slug.

The following sections describe the analytical models in some detail, including the model parameters and the fuel alloy properties, and then present the results of ALFUS validation. Finally, the stress–strain behavior of metal fuel pins is summarized.

3.23.4.2 Models in ALFUS

3.23.4.2.1 Calculation flow in ALFUS

The calculation flow in ALFUS is schematically shown in **Figure 22**. First, the temperature distribution in the fuel pin at time step $t = t_{n+1}$ is calculated from a linear power rate and a coolant flow rate at the present $t = t_{n+1}$, and from the slug–cladding gap and porosity in the slug at the previous time step $t = t_n$. Second, gas swelling and gas release are calculated based on the local temperature at $t = t_{n+1}$ and the stress state at $t = t_n$. After strain increments due to gas swelling, solid FP swelling, and thermal expansion
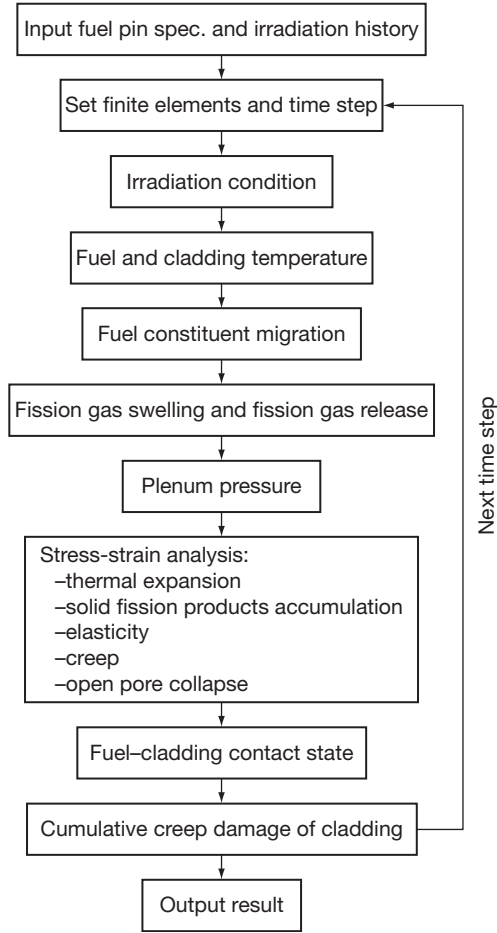
Figure 22 Calculation flow of ALFUS.

3.23.4.2.2 Stress–strain analysis model
3.23.4.2.2.1 Basic equations
Axial symmetric, r–z 2D finite element method is applied, which is successfully used in the LWR fuel performance code FEMAXI-III.[54] The virtual work principle with respect to a finite element (see Figure 23) yields

$$\int [B_n]^{\mathrm{T}}\{\sigma_{n+1}^i\}\mathrm{d}V + \int [B_n]^{\mathrm{T}}\{\mathrm{d}\sigma_{n+1}^{i+1}\}\mathrm{d}V = \{F_{n+1}\} \quad [19]$$

where F is the external force vector, $[B]$ is the node displacement–strain matrix, and $\{\sigma\} = \{\sigma_r, \sigma_\theta, \sigma_z, \tau_{rz}\}^{\mathrm{T}}$ is the stress vector. Superscript and subscript in eqn [19] represent the iteration counter in the Newton–Raphson iterative calculation and the time step, respectively, and 'd' denotes the corrective increment at the $i+1$th iteration at the present time t_{n+1}. In the parabolic isoparametric element used in this model (see Figure 23), the node displacement $\{u'\} = \{u_r', u_z'\}^{\mathrm{T}}$ within the element is interpolated as

$$u_r' = N_1 u_{1r} + N_2 u_{2r} + N_3 u_{3r} + N_4 u_{4r}$$

and

$$u_z' = N_1 u_{1z} + N_2 u_{2z} + N_3 u_{3z} + N_4 u_{4z} \quad [20]$$

where the element nodal displacement $\{u\} = \{u_{1r}, u_{1z}, u_{2r}, u_{2z}, u_{3r}, u_{3z}, u_{4r}, u_{4z}\}^{\mathrm{T}}$. The shape function N_i ($i = 1$ to 4) in eqn [20] is given by

$$N_1 = \frac{1}{4}(1-\xi)(1-\eta)$$

$$N_2 = \frac{1}{4}(1+\xi)(1-\eta)$$

$$N_3 = \frac{1}{4}(1+\xi)(1+\eta)$$

and

$$N_4 = \frac{1}{4}(1-\xi)(1+\eta) \quad [21]$$

where $-1 \le \xi \le 1$, $-1 \le \eta \le 1$. With the above shape function N_i, the node displacement–strain matrix $[B]$ can be expressed in accordance with Nakajima et al.[54] as

$$[B] = \begin{bmatrix} \frac{\partial N_1}{\partial r} & 0 & \frac{\partial N_2}{\partial r} & 0 & \frac{\partial N_3}{\partial r} & 0 & \frac{\partial N_4}{\partial r} & 0 \\ 0 & \frac{\partial N_1}{\partial z} & 0 & \frac{\partial N_2}{\partial z} & 0 & \frac{\partial N_3}{\partial z} & 0 & \frac{\partial N_4}{\partial z} \\ \frac{N_1}{r} & 0 & \frac{N_2}{r} & 0 & \frac{N_3}{r} & 0 & \frac{N_4}{r} & 0 \\ \frac{\partial N_1}{\partial z} & \frac{\partial N_1}{\partial r} & \frac{\partial N_2}{\partial z} & \frac{\partial N_2}{\partial r} & \frac{\partial N_3}{\partial z} & \frac{\partial N_3}{\partial r} & \frac{\partial N_4}{\partial z} & \frac{\partial N_4}{\partial r} \end{bmatrix} \quad [22]$$

during the time step interval $\Delta t = t_{n+1} - t_n$ are obtained, a new stress–strain state of the slug and the cladding are calculated by the Newton–Raphson scheme. Volume changes of the gas bubble and the open pore due to the stress state change are taken into account in the iterative calculation. The contact condition between the fuel slug and cladding is determined from the displacements of the slug outer surface and the cladding inner surface with consideration of the radial crack strain. The usual time step interval $\Delta t = 20$ h is thought to be sufficiently small compared with the time-scale of the in-reactor phenomena during steady-state irradiation. This preset time interval is divided into smaller intervals automatically in accordance with the rate of the slug–cladding gap closure and the creep rate of the hottest part of the slug. Such a time step control is essential when the stress–strain analysis is conducted for a high creep rate material like the U–Pu–Zr alloy.
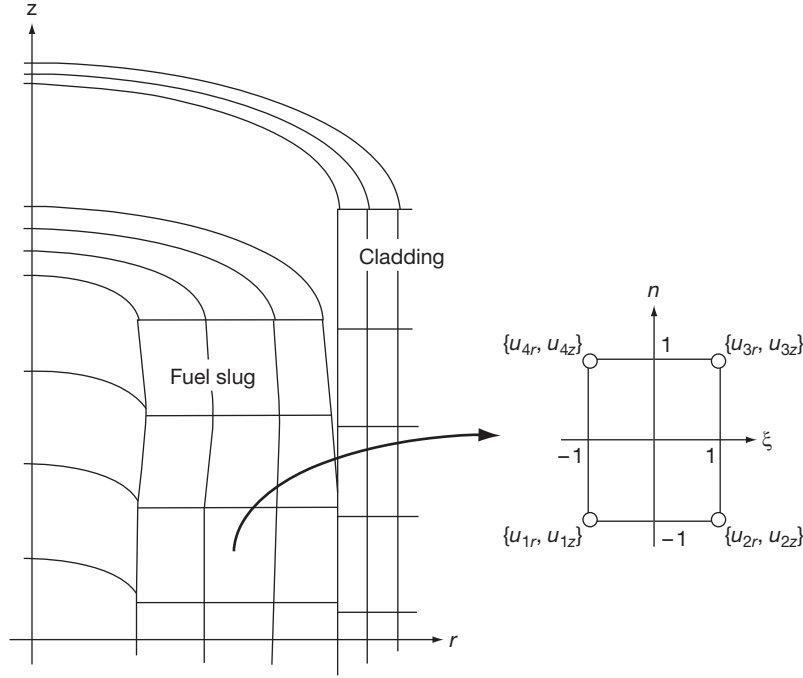
Figure 23 Finite element in the stress–strain analysis model.

Table 4 Strain components considered in ALFUS

Symbol	Strain component	Description
ε^{el}	Elastic	**Section 3.23.4.2.2.1**
ε^{th}	Thermal expansion	**Section 3.23.4.2.2.1**
ε^{sw}	Gas swelling $= \varepsilon^{\text{cls}} + \varepsilon^{\text{opn}}$	**Section 3.23.4.2.2.2**
ε^{cls}	Swelling due to closed bubbles	**Sections 3.23.4.2.2.2** and **3.23.4.2.3.2**
ε^{opn}	Swelling due to open pores $= \varepsilon^{\text{opn}+} + \varepsilon^{\text{opn}-}$	**Section 3.23.4.2.2.2**
$\varepsilon^{\text{opn}+}$	Open pore formation	**Sections 3.23.4.2.2.2** and **3.23.4.2.3.2**
$\varepsilon^{\text{opn}-}$	Open pore collapse	**Section 3.23.4.2.2.2**
ε^{cr}	Creep $+$ open pore collapse $= \varepsilon^{\text{creep}} + \varepsilon^{\text{opn}-}$	**Section 3.23.4.2.2.2**
$\varepsilon^{\text{creep}}$	Creep	**Section 3.23.4.2.2.2**
ε^{ss}	Solid FP swelling	**Section 3.23.4.2.5**

The derivatives $\partial N_i/\partial r$ and $\partial N_i/\partial z$ is given by

$$\left\{ \begin{array}{c} \frac{\partial N_i}{\partial r} \\ \frac{\partial N_i}{\partial z} \end{array} \right\} = [\mathcal{J}]^{-1} \left\{ \begin{array}{c} \frac{\partial N_i}{\partial \xi} \\ \frac{\partial N_i}{\partial \eta} \end{array} \right\} \quad [23]$$

where the Jacobian matrix $[\mathcal{J}]$ is given by

$$[\mathcal{J}] = \begin{bmatrix} \sum_{i=1}^{4} \frac{\partial N_i}{\partial \xi} r_i & \sum_{i=1}^{4} \frac{\partial N_i}{\partial \xi} z_i \\ \sum_{i=1}^{4} \frac{\partial N_i}{\partial \eta} r_i & \sum_{i=1}^{4} \frac{\partial N_i}{\partial \eta} z_i \end{bmatrix} \quad [24]$$

Considering the strain increments at the $i + 1$th iteration at the present time t_{n+1}, we can express the unknown variable $\left\{ d\sigma_{n+1}^{i+1} \right\}$ in eqn [19] as

$$([C_{\text{e}}] + [C_{\text{s}}] + [C_{\text{c}}]) \left\{ d\sigma_{n+1}^{i+1} \right\}$$
$$= [B_n] \left\{ \Delta u_{n+1}^{i+1} \right\} - [C_{\text{e}}] \left(\left\{ \sigma_{n+1}^{i} \right\} - \{\sigma_n\} \right)$$
$$- \left(\left\{ \Delta \varepsilon_{n+1}^{\text{th},i+1} \right\} + \left\{ \Delta \varepsilon_{n+1}^{\text{ss},i+1} \right\} + \left\{ \Delta \varepsilon_{n+1}^{\text{sw},i} \right\} + \left\{ \Delta \varepsilon_{n+1}^{\text{cr},i} \right\} \right) \quad [25]$$

where $\{u\}$ is the element nodal displacement and Δ means increment from the previous time t_n to the present t_{n+1}. Volumetric strain is represented by ε without $\{\}$ in the following text. Thermal expansion strain $\left\{ \Delta \varepsilon_{n+1}^{\text{th},i+1} \right\}$ is given as a function of temperature. Components of strain vector $\{\varepsilon\}$ are summarized in **Table 4**. Substituting eqn [25] into eqn [19] to eliminate

$\left\{d\sigma_{n+1}^{i+1}\right\}$, we can obtain the solution $\left\{\Delta u_{n+1}^{i+1}\right\}$. Then, the stress vector and each component of the strain at the time step $t = t_{n+1}$ is calculated after the $i + 1$th iteration. The stress–strain matrices $[C_e]$ and $[C_s]$ correspond to the elasticity of the fuel alloy and volumetric change of closed gas bubbles, respectively. The other stress–strain matrix $[C_c]$ represents the response by creep of the fuel alloy and volume decrease of the open pores. Each stress–strain matrix is given as follows.

For the elastic strain–stress matrix $[C_e]$,

$$\left\{\Delta\varepsilon_{n+1}^{el,i+1}\right\} \equiv \left\{\Delta\varepsilon_{n+1}^{el,i}\right\} + [C_e]\left\{d\sigma_{n+1}^{i+1}\right\}$$

$$[C_e] = \begin{bmatrix} \frac{1}{E} & -\frac{\nu}{E} & -\frac{\nu}{E} & 0 \\ -\frac{\nu}{E} & \frac{1}{E} & -\frac{\nu}{E} & 0 \\ -\frac{\nu}{E} & -\frac{\nu}{E} & \frac{1}{E} & 0 \\ 0 & 0 & 0 & \frac{2(1+\nu)}{E} \end{bmatrix} \quad [26]$$

where E is the elastic modulus and ν is the Poisson's ratio. The stress–strain matrix $[C_s]$ in eqn [25] for the volume change of closed gas bubbles is defined as

$$\left\{d\varepsilon_{n+1}^{sw,i+1}\right\} \equiv [C_s]\left\{d\sigma_{n+1}^{i+1}\right\}$$

$$\left(\equiv \left\{\Delta\varepsilon_{n+1}^{sw,i+1}\right\} - \left\{\Delta\varepsilon_{n+1}^{sw,i}\right\}\right) \quad [27]$$

As described in **Section 3.23.4.2.3**, the volume of a closed gas bubble (class i) is calculated by the Van der Waals equation:

$$\left(\sigma_m + \frac{2\gamma}{r_i}\right)\left(\frac{4}{3}\pi r_i^3 - m_i A_v \beta\right) = m_i RT \quad [28]$$

where γ is the surface tension (N m^{-1}), r_i the radius of a class i bubble (m), m_i the gas amount in a class i bubble (mol), A_v the Avogadro number (atoms mol^{-1}), R gas constant (J K^{-1} mol^{-1}), T the temperature (K), $\beta = 85 \times 10^{-30}$ (m^3), and σ_m the average stress:

$$\sigma_m = \frac{\sigma_r + \sigma_\theta + \sigma_z}{3} \quad [29]$$

Differentiation of eqn [28] yields

$$-\frac{dr_i}{d\sigma_m} = \frac{r_i^3 - \frac{3}{4\pi}m_i A_v \beta}{3r_i^2\sigma_m + 4\gamma r_i + 2\gamma\frac{3}{4\pi}m_i A_v \beta/r_i^2} \quad [30]$$

When we consider the volume change of one gas bubble,

$$\frac{d\varepsilon_i^{sw}}{d\sigma_m} = \frac{d\varepsilon_i^{sw}}{dr_i}\frac{dr_i}{d\sigma_m}$$

and

$$\frac{d\varepsilon_i^{sw}}{dr_i} = 4\pi r_i^2 C_i \quad [31]$$

where C_i is the number density (n m^{-3}) of the class i bubble. From eqns [27], [30], and [31],

$$[C_s] = \sum_i \frac{1}{3}\frac{d\varepsilon_i^{sw}}{d\sigma_m}\begin{bmatrix} \frac{1}{3} & \frac{1}{3} & \frac{1}{3} & 0 \\ \frac{1}{3} & \frac{1}{3} & \frac{1}{3} & 0 \\ \frac{1}{3} & \frac{1}{3} & \frac{1}{3} & 0 \\ 0 & 0 & 0 & 0 \end{bmatrix}$$

$$= \frac{4\pi r_i^2(r_i^3 - \frac{3}{4\pi}m_i A_v\beta)C_i}{27r_i^2\sigma_m + 36\gamma r_i + 18\gamma\frac{3}{4\pi}m_i A_v\beta/r_i^2}$$

$$\begin{bmatrix} 1 & 1 & 1 & 0 \\ 1 & 1 & 1 & 0 \\ 1 & 1 & 1 & 0 \\ 0 & 0 & 0 & 0 \end{bmatrix} \quad [32]$$

The stress–strain matrix $[C_c]$ in eqn [25] for the creep deformation is defined as

$$\left\{\Delta\varepsilon_{n+1}^{cr,i+1}\right\} \equiv \left\{\Delta\varepsilon_{n+1}^{cr,i}\right\} + [C_c]\left\{d\sigma_{n+1}^{i+1}\right\}$$

$$= \Delta t_{n+1}\left\{\dot{\varepsilon}_{n+\theta}^{c,i+1}\right\} \quad [33]$$

where the time increment $\Delta t_{n+1} = t_{n+1} - t_n$, and $\left\{\dot{\varepsilon}_{n+\theta}^{c,i+1}\right\}$ is the creep strain rate vector at a stress $\{\sigma_{n+\theta}\}$ estimated at a time $t_{n+\theta} = t_n + \theta(t_{n+1} - t_n)$, $(0 \leq \theta \leq 1)$. According to Nakajima et al.,[54] the matrix $[C_c]$ is given by

$$[C_c] = \theta\Delta t_{n+1}\left(F_1\left[\sigma_j'\sigma_k'\right]_{n+\theta}^i + F_2\left[\frac{\partial\sigma_j'}{\partial\sigma_k}\right]_{n+\theta}^i\right)$$

$$F_1 = \frac{9}{4\left(\overline{\sigma}_{n+\theta}^i\right)^2}\left(\left(\frac{\partial f}{\partial\overline{\sigma}}\right)_{n+\theta}^i - \frac{f_{n+\theta}^i}{\overline{\sigma}_{n+\theta}^i}\right) \quad [34]$$

$$F_2 = \frac{3f_{n+\theta}^i}{2\overline{\sigma}_{n+\theta}^i}$$

where the function f is the uniaxial creep strain rate of the fuel alloy given by eqn [38]; $f = \dot{\varepsilon}^c(\overline{\sigma})$. The equivalent stress $\overline{\sigma}$ is given by eqn [39], and the deviatoric stress $\{\sigma'\}$ is defined as

$$\{\sigma'\} = \frac{2\overline{\sigma}}{3}\left\{\frac{\partial\overline{\sigma}}{\partial\sigma}\right\} \quad [35]$$

Note that $\left\{\Delta\varepsilon_{n+1}^{cr,i+1}\right\}$ in eqn [33] includes the strain increment for the volume decrease of the open pores, as shown in the next section.

3.23.4.2.2.2 Volume decrease of the open pores

Total swelling increment $\{\Delta\varepsilon^{\text{sw}}\}$ (hereinafter, iteration and time step counters are dropped) in eqn [25] is defined as

$$\{\Delta\varepsilon^{\text{sw}}\} = \{\Delta\varepsilon^{\text{cls}}\} + \{\Delta\varepsilon^{\text{opn}}\},$$
$$\{\Delta\varepsilon^{\text{opn}}\} = \{\Delta\varepsilon^{\text{opn+}}\} + \{\Delta\varepsilon^{\text{opn-}}\} \qquad [36]$$

The vector $\{\Delta\varepsilon^{\text{cls}}\}$ is the isotropic strain increment due to the closed bubble development, and $\{\Delta\varepsilon^{\text{opn}}\}$ is the 'net' isotropic strain increment due to open pore volume change, which consists of two components: $\{\Delta\varepsilon^{\text{opn+}}\}$ and $\{\Delta\varepsilon^{\text{opn-}}\}$. The increment $\{\Delta\varepsilon^{\text{opn+}}\}$ corresponds to open pore increase by interconnection of the closed bubbles. The gas swelling model explained later gives $\{\Delta\varepsilon^{\text{cls}}\}$ and $\{\Delta\varepsilon^{\text{opn+}}\}$. The increment $\{\Delta\varepsilon^{\text{opn-}}\}$ means the open pore collapse, which is calculated with creep strain increment $\{\Delta\varepsilon^{\text{cr}}\}$ as follows. Since the open pore has connection with the external of the slug and does not include high-pressure fission gas unlike the closed bubble, it may collapse when compressive stress is applied. Here, volume decrease due to the open pore collapse is assumed to be controlled by creep mechanism and calculated in a manner similar to the hot press model proposed by Rashid et al.[55] When the creep strain component without volume change is denoted by $\{\Delta\varepsilon^{\text{creep}}\}$, the sum of $\{\Delta\varepsilon^{\text{opn-}}\}$ and $\{\Delta\varepsilon^{\text{creep}}\}$ is expressed by the following flow rule:

$$\{\Delta\varepsilon^{\text{cr}}\} \equiv \{\Delta\varepsilon^{\text{creep}}\} + \{\Delta\varepsilon^{\text{opn-}}\}$$
$$= \dot{\bar{\varepsilon}}^{\text{c}}(\bar{\sigma})\left\{\frac{\partial\bar{\sigma}}{\partial\sigma_i}\right\}\Delta t \qquad [37]$$

where $\dot{\bar{\varepsilon}}^{\text{c}}(\bar{\sigma})$ is the equivalent creep strain rate and σ_i $(i = r, \theta, z)$ is the stress in the slug. The stress σ_i takes a negative value when it is compressive. The equivalent creep strain rate for the U–Pu–Zr ternary alloy is given by

$$\dot{\bar{\varepsilon}}^{\text{c}}(\bar{\sigma}) = \begin{cases} (5000\bar{\sigma} + 6.0\bar{\sigma}^{4.5})\text{e}^{-52\,000/RT} & \leq 923\text{K} \\ 0.08\bar{\sigma}^3\ \text{e}^{-28\,500/RT} & > 923\text{K} \end{cases} \qquad [38]$$

according to Gruber and Kramer.[56] The equivalent stress $\bar{\sigma}$ in eqn [37] is given by

$$\bar{\sigma} = \left[\frac{1}{2}((\sigma_r - \sigma_\theta)^2 + (\sigma_\theta - \sigma_z)^2 + (\sigma_z - \sigma_r)^2\right.$$
$$\left. + 6\tau_{rz}) + 3\alpha(\sigma_r + \sigma_\theta + \sigma_z + 3P_{\text{pl}})^2\right]^{1/2} \qquad [39]$$

where the shear stress τ_{rz} is usually negligible. The term $(\sigma_r + \sigma_\theta + \sigma_z + 3P_{\text{pl}})$ represents the net effective

hydrostatic stress applied to the open pores because the gas plenum pressure P_{pl} in eqn [39] is equal to the 'internal' pressure of the open pores. The hot press parameter α means the compressibility of the open pores. Substituting eqn [39] into eqn [37], we obtain

$$\{\Delta\varepsilon^{\text{cr}}\} = \frac{\dot{\bar{\varepsilon}}^{\text{c}}(\bar{\sigma})}{2\bar{\sigma}}\Delta t$$

$$\begin{bmatrix} 2+6\alpha & -1+6\alpha & -1+6\alpha & 18\alpha \\ -1+6\alpha & 2+6\alpha & -1+6\alpha & 18\alpha \\ -1+6\alpha & -1+6\alpha & 2+6\alpha & 18\alpha \end{bmatrix}\begin{Bmatrix} \sigma_r \\ \sigma_\theta \\ \sigma_z \\ P_{\text{pl}} \end{Bmatrix} \qquad [40]$$

In eqn [40], the value of $-1 + 6\alpha$ must be negative. (For example, consider the case of $\{\sigma\}^{\text{T}} = \{\sigma_r, 0, 0, 0\}$. The sign of $\Delta\varepsilon_\theta^{\text{cr}}$ must be opposite to that of σ_r.) Therefore, α should be in the range of $0 \leq \alpha \leq 1/6$. The hot press parameter α is assumed to be dependent on the open pore swelling $\varepsilon_{\text{sw}}^{\text{opn}}$ and takes the maximum value when $\varepsilon_{\text{sw}}^{\text{opn}}$ is as large as 10%:

$$\alpha = \begin{cases} 0.0, & \varepsilon_{\text{sw}}^{\text{opn}} = 0 \\ \dfrac{1}{6}\left(\dfrac{\varepsilon_{\text{sw}}^{\text{opn}}}{0.1}\right)^{1.5}, & 0 < \varepsilon_{\text{sw}}^{\text{opn}} < 0.1 \\ 1/6, & 0.1 \leq \varepsilon_{\text{sw}}^{\text{opn}} \end{cases} \qquad [41]$$

The dependency of α on $\varepsilon_{\text{sw}}^{\text{opn}}$ was determined on the basis of the following consideration of the compressibility of the porous material which consists of the same-sized spherical shells (see **Figure 24**).

When hydrostatic pressure P_{ex} is applied to the porous material as shown in **Figure 24**, the equivalent
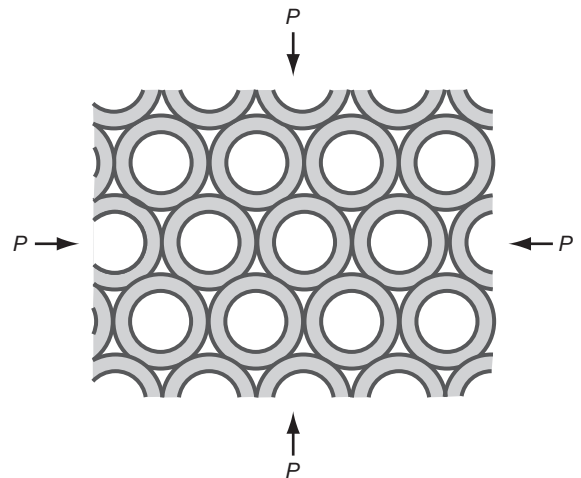

Figure 24 Closely-packed spherical shells, forming porous material.

stress $\bar{\sigma}_{pm}$ in this material can be expressed according to eqn [39] as

$$\bar{\sigma}_{pm} = 3\sqrt{3}\alpha(P_{ex} - P_{in}) \qquad [42]$$

where P_{in} is internal pressure in the central pore ($P_{ex} > P_{in}$). Substituting eqn [39] into eqn [37] and using eqn [42], we obtain the following volumetric strain rate $\dot{\varepsilon}_V^c$:

$$\dot{\varepsilon}_V^c = -3\sqrt{3}\alpha\dot{\bar{\varepsilon}}^c(\bar{\sigma}_{pm}) \qquad [43]$$

On the other hand, if each shell itself is made of dense material, the creep deformation rate of the shell under hydrostatic pressure P_{ex} is described by $\alpha = 0$ in eqn [39]. The volumetric strain rate of the whole shell including the central pore is expressed as

$$\dot{\varepsilon}_V^c = -3\dot{\bar{\varepsilon}}^c(\bar{\sigma}_{sh}) \qquad [44]$$

The equivalent stress $\bar{\sigma}_{sh}$ at the outer surface of the shell ($r = r_2$) is given by

$$\bar{\sigma}_{sh} = \frac{3}{2}\varepsilon_{pore}(P_{ex} - P_{in}), \varepsilon_{pore} = \frac{r_1^3}{r_2^3 - r_1^3} \qquad [45]$$

where r_1 is the central pore radius and ε_{pore} means the volume ratio of the central pore to the dense material. When the interstitial media between the shells is assumed to transmit the forces but not to contribute to the volumetric strain of the whole material,[55] the volumetric strain rate of eqn [43] is equal to that of eqn [44]. When a creep rate of the dense material of the shell is assumed to be expressed in the form of

$$\dot{\bar{\varepsilon}}^c = A\sigma^n, A : \text{constant} \qquad [46]$$

coupling eqn [43] with eqn [44] yields

$$\alpha = \frac{1}{3}\left(\frac{\varepsilon_{pore}}{2}\right)^{\frac{2n}{n+1}} \qquad [47]$$

The index $2n/(n+1)$ in eqn [47] takes a value of ~ 1.5, since the creep rate correlation for U–Pu–Zr alloys used in ALFUS has the stress dependence of $n = 3$ for the γ-solid solutions (>923 K) and $n = 3$–4.5 for the lower temperature, as expressed in eqn [38]. Equation [41] is obtained by adjusting eqn [47] so that α takes the value of 1/6 at $\varepsilon_{sw}^{opn} = 0.1$. The idealized model described earlier is considered applicable to the limiting case that the open pores are almost collapsed and 'closed,' namely $\varepsilon_{sw}^{opn} \to 0$.

McDeavitt[57] conducted hot isotropic pressing (HIP) experiments at 973 K for porous U–10 wt% Zr specimens produced by sintering U and Zr powders. Linear strain rates of the specimens were measured in those experiments. The results for the 'metal-derived specimens'[57] are summarized in Table 5. The U–Zr specimens included closed pores in which internal pressure was equilibrated with the sintering pressure. The HIP stress, which was sufficiently higher than the closed pore pressure, is applied to the specimens with pressurized Ar gas. During the HIP process, the volume of the closed pores in the specimens decreased, while the volume of the open pores was thought almost constant because the pressurized Ar gas was in the open pore. Therefore, the volume fraction of the closed pores shown in Table 5 corresponds to that of the open pores in the ALFUS model. The range of the fractional closed pore in Table 5 can be interpreted to be the open pore swelling of $0.015 \le \varepsilon_{sw}^{opn} \le 0.1$. Applying eqns [37] and [39] to the porous U–Zr specimens, the measured linear strain rate $-\dot{\varepsilon}_l$ is expressed as

$$-\dot{\varepsilon}_l = \frac{-\dot{\varepsilon}_V^c}{3} = \sqrt{3}\alpha\dot{\bar{\varepsilon}}^c(\bar{\sigma}_{HIP}) \qquad [48]$$

Creep strain rate $\dot{\bar{\varepsilon}}^c$ for U–(Pu–)Zr alloys at 973 K is given in McDeavitt[57] by

$$\dot{\bar{\varepsilon}}^c = 3.2 \times 10^{-8}\bar{\sigma}_{HIP}^3 \qquad [49]$$

Table 5 Result of HIP experiment for sintered U–Zr alloys

Specimen	Driving force (MPa)	Linear strain Rate[a] (/s)	Fractional closed pore[b](%)	α
M9	15.5	2.50E−06	5.3	0.0093
M10	8.9	2.50E−07	9.8	0.0067
M13	20.7	7.00E−06	3.2	0.0101
M15	12.4	1.20E−06	1.5	0.0090
M18	12.4	1.20E−06	5.2	0.0090
M20	19.4	7.00E−06	6.4	0.0111
M22	5.7	3.00E−08	9.8	0.0046

[a]Read from plot data in McDeavitt[57]
[b]Calculated from data reported in McDeavitt[57] by (% closed porosity)/(100-(% closed porosity)).

which is essentially identical to eqn [38]. The equivalent stress $\bar{\sigma}_{HIP}$ in eqn [48] is given in the form similar to eqn [42]:

$$\bar{\sigma}_{HIP} = 3\sqrt{3\alpha}P_{eff} \qquad [50]$$

where P_{eff} is the HIP driving force in **Table 5**. Substitution of eqns [49] and [50] into eqn [48] gives the hot press parameter:

$$\alpha = \sqrt{\frac{-\dot{\varepsilon}_l}{7.8 \times 10^{-6}P_{eff}^3}} \qquad [51]$$

Values of α calculated from eqn [51] are also presented in **Table 5**, which indicates that α is in the range from 1/220 to 1/90. Although the function of eqn [41] gives larger α values than this range, eqn [41] seems acceptable because the open pore in the irradiated fuel slug is really 'open' to the outside of the slug and considered more compressible than the closed pore in the sintered U–Zr specimen.

3.23.4.2.3 Gas swelling model

The gas swelling model gives the strain increments $\{\Delta\varepsilon^{cls}\}$ and $\{\Delta\varepsilon^{opn+}\}$ in eqn [36] due to the closed bubble and open pore formation, respectively, and also calculates the amount of fission gas released into the gas plenum. This swelling model, which was applicable to analysis of uranium metal swelling,[58] was modified and incorporated into the ALFUS code.[53]

This gas swelling model comprises two parts (see **Figure 25**); One of the submodels describes migration of fission gas atoms and intragranular gas bubbles into the grain or phase boundary (intragranular gas model). Another submodel describes growth of the grain-boundary bubbles due to gas supply from the grain and coalescence with the existing grain-boundary bubbles (grain-boundary gas model). The open pore formation due to interconnection of the grain-boundary (closed) bubbles and fission gas release through the open pore are also treated in this submodel. Gas swelling volume is calculated as the total volume of the closed bubbles and the open pores.

3.23.4.2.3.1 Intragranular gas model

The intragranular gas model for oxide fuel by Wood and Matthews[59] is modified and applied to calculate the concentrations of the fission gas atoms and the gas bubbles in the grain. The following assumptions are made in this model:

(a) A part of the gas atoms generated by fission forms gas bubbles in the grain. Some gas atoms may be trapped by the existing gas bubbles. Some of the gas bubbles may be destroyed by a fission fragment and dissolved in the fuel alloy matrix. Fission gas atoms and gas bubbles migrate in the spherical grain by the diffusion mechanism (**Figure 25**).
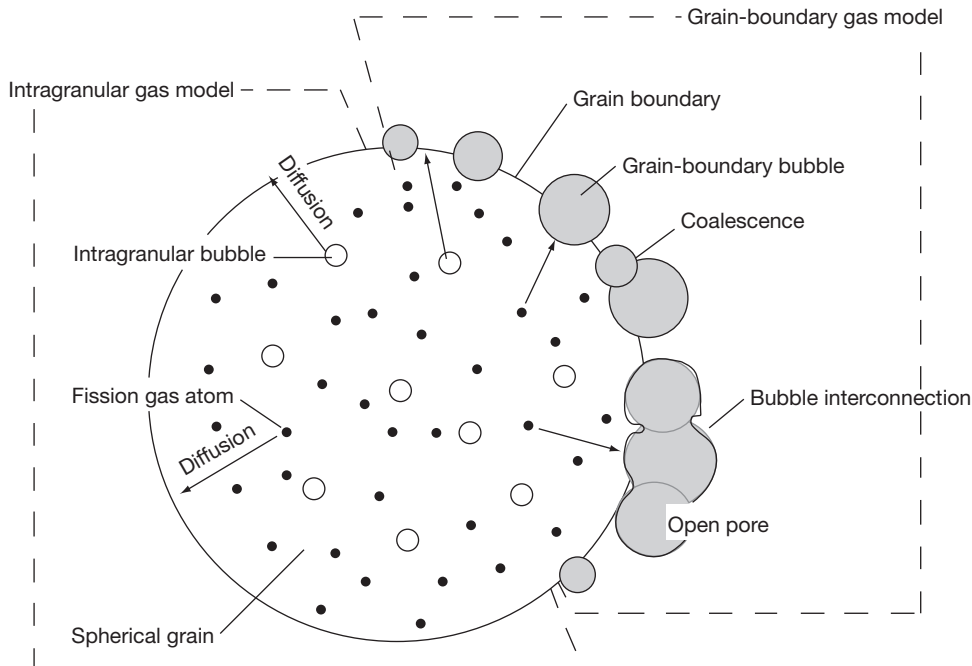

Figure 25 Concept of gas swelling model in ALFUS.

The number density of the gas bubbles is represented by a single bubble size.

(b) The gas bubble formation (nucleation), gas atom trapping by the gas bubbles, and the resolution of the gas into the matrix are in an equilibrium state.

(c) The gas atoms and bubbles that arrive at the grain boundary form the grain-boundary bubbles or flow into the existing grain-boundary bubbles, and do not come back to the grain. This means that the concentrations of both the gas atoms and the intragranular bubbles are zero at the boundary.

According to Wood and Matthews,[59] assumption (a) is expressed as

$$\frac{\partial C_g}{\partial t} = \frac{1}{r^2}\frac{\partial}{\partial r}\left(D_g r^2 \frac{\partial C_g}{\partial r}\right) + K_g - D_g k_b^2 C_g$$
$$- KC_t + bC_{gb} \qquad [52]$$

$$A_v m_0 \frac{\partial C_b}{\partial t} = A_v m_0 \frac{1}{r^2}\frac{\partial}{\partial r}\left(D_{gb} r^2 \frac{\partial C_b}{\partial r}\right)$$
$$+ D_g k_b^2 C_g + KC_t - bC_{gb} \qquad [53]$$

where C_g is the concentration of fission gas atoms dissolved in the matrix (atoms m^{-3}); C_{gb}, the concentration of gas included in intragranular bubbles (atoms m^{-3}), $C_{gb} = A_v m_0 C_b$; C_b, the number density of intragranular bubbles (bubbles m^{-3}), $C_t = C_g + C_{gb}$; A_v, the Avogadro number (atoms mol^{-1}); m_0, the gas amount in one intragranular bubble (mol); D_g, the diffusion coefficient of the fission gas atom (m^2 s^{-1}); D_{gb}, the diffusion coefficient of the intragranular bubble (m^2 s^{-1}); K_g, the generation rate of the fission gas atoms (atoms m^3 s^{-1}); $D_g k_b^2 C_g$, the rate of gas atom trapping by the bubble (atoms m^{-3} s^{-1}); KC_t, the bubble nucleation rate (atoms m^{-3} s^{-1}); and bC_{gb} the rate of the bubble resolution by the fission fragment (atoms m^{-3} s^{-1}).

Wood and Matthews[59] assumed that the gas bubbles were immobile for the oxide fuel, so that the first term in the right-hand side of eqn [53] was not included in the equation. In metal fuel, however, the diffusion of gas bubbles will not be negligible, because the ratio T/T_m of the fuel temperature T (on average) to the melting temperature T_m for metal fuel is higher than that for the oxide fuel.

From assumption (b),

$$D_g k_b^2 C_g + KC_t = bC_{gb} \qquad [54]$$

Values of K and b were estimated as $K = 4 \times 10^{-3}$ (s^{-1}) and $b = 6 \times 10^{-2}$ (s^{-1}) based on Wood and Matthews.[59] The sink strength k_b^2 of bubbles for the

migrating gas atoms is expressed in Wood and Matthews[59] as

$$k_b^2 = 4\pi r_b \bar{C}_b \qquad [55]$$

Here, $\bar{C}_b$ is estimated from the number density of the bubbles at the previous time step. The radius of the bubble r_b in eqn [55] is calculated by the Van der Waals equation (see eqn [28]), assuming an equilibrium state among internal pressure, surface tension, and external stress (average stress in the fuel slug) of the bubble. The gas amount m_0 in the bubble was assumed to be $m_0 = 1 \times 10^{-22}$ so that the bubble radius r_b takes a value of $\sim$1 nm. From eqn [54],

$$C_g = \frac{b - K}{D_g k_b^2 + b}C_t, \text{ and } C_{gb} = \frac{D_g k_b^2 + K}{D_g k_b^2 + b}C_t \qquad [56]$$

Coupling eqns [52], [53], and [56] yields

$$\frac{\partial C_t}{\partial t} = \frac{1}{r^2}\frac{\partial}{\partial r}\left((D_1 + D_2)r^2\frac{\partial C_t}{\partial r}\right) + K_g \qquad [57]$$

where

$$D_1 = \frac{b - K}{D_g k_b^2 + b}D_g, D_2 = \frac{D_g k_b^2 + K}{D_g k_b^2 + b}D_{gb} \qquad [58]$$

During normal reactor operation, change in the irradiation conditions, such as fission rate and temperature, is much slower than diffusion of the gas atom and the bubble, so the system can be assumed to be in a steady-state: $\partial C_t/\partial t = 0$. The diffusion equation [57] can be solved under the boundary conditions: $C_t = 0$ at the grain boundary ($r = r_G$, assumed to be 2 µm) from assumption (c), and $\partial C_t/\partial r = 0$ at the center of the spherical grain ($r = 0$). In ALFUS, the approximate numerical solution is used that Matthews and Wood[60] proposed.

The diffusion coefficient D_g of the gas atom in eqns [52] and [53] is tentatively assumed to be equal to the self-diffusion coefficient of γ-uranium[61]:

$$D_g = 1.19 \times 10^{-7}\exp\left(-\frac{26700}{RT}\right) \qquad [59]$$

because no data on diffusion of the noble gas atom in metals is available. The diffusion coefficient D_{gb} of the intragranular bubble in eqn [53] can be related to the surface diffusion coefficient D_s of the bubble inner surface by considering the jump distance of a bubble due to individual jumps of molecules on its inner surface,[62] which yields a form of

$$D_{gb} = C_{adj}\frac{3}{2\pi}\left(\frac{a_0}{r_b}\right)^4 D_s \qquad [60]$$

where a_0 is the lattice constant of the fuel alloy ($=3.0\times10^{-10}$ m). The surface diffusion coefficient D_s of the fuel alloy in eqn [60] is assumed to be $D_s = 1000D_g$, which gives the value close to the correlation evaluated by Gruber and Kramer.[63] The parameter C_{adj} in eqn [60] was introduced to account for various factors affecting the gas bubble migration, such as fission fragments, multiphase structures of the fuel alloy, and an internal gas pressure in the bubble. The value of C_{adj} was adjusted as described in **Section 3.23.4.2.8**; $C_{adj} = 20$. In this case, $D_{gb} \approx 77D_g$ for the intragranular bubble.

As far as eqn [59] is used, D_g takes a value in the range of $\sim 10^{-13}$ to $\sim 10^{-15}$, and $C_b \sim 10^{-15}$ to $\sim 10^{-16}$ in the analyses of EBR-II test fuels and the prototypic fuel. Therefore, the value of $D_g k_b^2$ is on the order of $\sim 10^{-6}$ ($\ll b$), so that the gas concentrations in the form of the gas atoms and bubbles can be estimated from eqn [56] as

$$C_g \approx \left(1 - \frac{K}{b}\right)C_t \approx 0.93C_t \text{ and } C_{gb} \approx \frac{K}{b}C_t \qquad [61]$$
$$\approx 0.07C_t$$

Therefore, the ratio of fission gas transfer by the gas atom diffusion to that by the bubble diffusion can be estimated as

$$\frac{D_g\left(\partial C_g/\partial r\right)_{r=r_G}}{D_{gb}\left(\partial C_{gb}/\partial r\right)_{r=r_G}} \approx \frac{D_g 0.93(\partial C_t/\partial r)_{r=r_G}}{77D_g 0.07(\partial C_t/\partial r)_{r=r_G}} \approx 0.17$$
$$[62]$$

This indicates that $\sim 15\%$ of the total fission gas generated within the grain is transferred by the bubble migration, and this value is relatively independent of the temperature.

3.23.4.2.3.2 Grain-boundary gas model
3.23.4.2.3.2.1 Grain-boundary bubble (closed bubble)   This submodel describes growth of the grain-boundary bubble, the open pore formation, and fission gas release through the open pore. The following assumptions are made in this grain-boundary bubble model (see **Figure 25**):

(d) The grain-boundary bubbles coalesce with each other by collision due to their random migration. They also absorb the fission gas atoms diffusing out from the grain. These two processes increase the size of the grain-boundary bubble. The intragranular gas bubbles coming out from the grain form the smallest grain-boundary bubbles.

(e) When the volume fraction of the grain-boundary bubbles increases over a threshold value, they begin interconnecting and form the open pore.

(f) When the bubbles interconnect and form the open pore, the fission gas included in the bubbles is immediately released into the gas plenum. The intragranular and grain-boundary bubbles may collide with the open pore. It leads to gas release and increase in an open pore size. The fission gas atoms may also be released through the open pore.

The grain-boundary (closed) bubbles are classified into $M - 1$ classes by gas amount m_i (mol) included in each bubble so that growth of the bubbles can be numerically described. Although the characteristics of the open pore will be different from that of the closed bubble, the open pore is categorized into the class M 'bubble' for the convenience of numerical modeling. The formation of the open pore (bubble interconnection) is, however, treated in a manner different from the growth of the closed bubble, as mentioned later.

The change in the number density of the closed bubble of class i can be described by considering fission gas supply from the grain, growth of lower $(i - 1)$ class bubbles, growth to upper class $(i + 1)$ bubbles, and collision with upper class bubbles (assumption (d));

$$\frac{dC_1}{dt} = G_1 - R'_{i,j} - \sum_{j=1}^{M} R_{j,1}, \quad i = 1 \qquad [63]$$

$$\frac{dC_i}{dt} = G_i + \sum_{j=1}^{i-1} R'_{i-1,j} - \sum_{j=1}^{i} R'_{i,j}$$
$$- \sum_{j=i}^{M} R_{j,i}, \quad i = 2 \text{ to } M - 2 \qquad [64]$$

where C_i is the number density of class i bubble, G_i is the increased rate of the number density of the class i bubble by fission gas transfer from the grain, $R_{i,j}$ is the collision rate of class i with class j bubble, and $R'_{i,j}$ is the rank-up rate from class i to class $i + 1$ by coalescence with class j bubble. The term G_i $(i > 1)$ in eqns [63] and [64] is calculated by distributing the fission gas atom from the grain in proportion to the grain surface area occupied by each class bubble. The term G_1 is calculated from the amount of gas in the intragranular bubbles arriving at the boundary (assumption (d)). According to Hayns and Wood,[64] $R_{i,j}$ and $R'_{i,j}$ can be expressed as

$$R_{i,j} = 4\pi\delta(D_i + D_j)(r_i + r_j)C_iC_j \qquad [65]$$

$$R'_{i,j} = 4\pi\delta(D_i + D_j)(r_i + r_j)C_iC_jF_{i,j} \qquad [66]$$

$$\delta = \begin{cases} 1/2: & i = j \\ 1: & i \neq j \end{cases}$$

where r_i is the radius of class i bubble and D_i is the diffusion coefficient of class i bubble. The factor $F_{i,j}$ in eqn [66] means a fraction of the class i bubbles which rank up to the upper class $(i + 1)$ when one class i bubble collides with the lower class (j) bubble, and can be given by the conservation of the amount of the bubble gas:

$$m_i + m_j = (1 - F_{i,j})m_i + F_{i,j}m_{i+1}. \qquad [67]$$

The diffusion coefficients D_i in eqns [65] and [66] should be determined by considering the characteristics of the grain or phase boundary. However, the bubble mobility on the boundary in the fuel alloy is not known well at this stage. It was assumed, therefore, that D_i is given by eqn [60].

3.23.4.2.3.2.2 Open pore   The formulation similar to eqns [63]–[67] was assumed for the open pore formation by interconnection of the gas bubbles. For the class $M - 1$ bubble (the highest class of the closed bubble) and the class M 'bubble' (the open pore),

$$\frac{dC_{M-1}}{dt} = G_{M-1} + \sum_{j=1}^{M-2} R'_{M-2,j}$$
$$- \sum_{j=1}^{M-1} R'_{M-1,j} - \sum_{j=M-1}^{M} R_{j,M-1} \qquad [68]$$

$$\frac{dC_M}{dt} = G_M + \sum_{j=1}^{M-1} R''_{M-1,j} + \sum_{j=1}^{M-1} R'_{M,j} \qquad [69]$$

$$R'_{M-1,j} = 4\pi\delta(D_{M-1} + D_j)$$
$$(r_{M-1} + r_j)C_{M-1}C_j F'_{M-1,j} \qquad [70]$$

$$R''_{M-1,j} = 4\pi\delta(D_{M-1} + D_j)$$
$$(r_{M-1} + r_j)C_{M-1}C_j F_{M-1,j} f_{M-1,j} \qquad [71]$$

$$R'_{M,j} = 4\pi\delta(D_M + D_j)(r_M + r_j)C_M C_j F_{M,j} \qquad [72]$$

The second term in the right-hand side of eqn [69] represents the open pore formation by interconnection between the grain-boundary bubbles. The first and third terms indicate evolution of the existing open pores by the fission gas supply from the grain and by coalescence with the grain-boundary bubbles, respectively. For the values of m_i assumed currently (see Section 3.23.4.2.8), $D_M \approx D_{M-1} \ll D_{M-2}$ and $R'_{M,M-1} \ll R'_{M,M-2}$, which means that the open pores are treated as immobile pores.

Based on assumption (e), F-factors in eqns [70]–[72] are different from that determined by eqn [67]

as follows. Since the open pore is treated as the highest-class (M) bubble, the factor $F_{M,j}$ in eqn [72] is given by the following conservation of gas amount:

$$m_M + m_j = m_M + F_{M,j}m_M \qquad [73]$$

Note that 'gas amount' m_M of the open pore is the input parameter that controls the rate of rank-up of the closed bubble to the open pore. The value of m_M was adjusted so that the fission gas release data can be reproduced, as explained in **Section 3.23.4.2.8**. The factor $F'_{M-1,j}$ in eqn [70] represents the fraction of the bubble interconnection to coalescence of one class j bubble with the class $M - 1$ bubble. When every coalescence of the class j bubble with the class $M - 1$ bubble contributes to the open pore formation (the bubble interconnection, i.e., rank-up to the class M), the conservation of gas amount included in the bubbles is expressed as

$$m_{M-1} + m_j = (1 - F_{M-1,j})m_{M-1} + F_{M-1,j}m_M \qquad [74]$$

where $F_{M-1,j}$ is essentially the same as $F_{i,j}$ in eqn [67]. In this case, $F'_{M-1,j} = F_{M-1,j}$. On the other hand, when gas swelling is not enough to form the open pore and a part of the coalescence with the class $M-1$ bubble contributes only to increase of the number density of the class $M - 1$ bubbles, the gas amount conservation is expressed as

$$m_{M-1} + m_j = (1 - F'_{M-1,j})m_{M-1}$$
$$+ F_{M-1,j}f_{M-1,j}m_M \qquad [75]$$

The factor $F'_{M-1,j}$ is calculated by coupling eqn [74] with eqn [75]. The function $f_{M-1,j}$ can be considered as a probability of open pore formation. It appears reasonable to assume that the probability $f_{M-1,j}$ increases with the gas swelling level. In this study, $f_{M-1,j}$ is given by

$$f_{M-1,j} = \begin{cases} 0.0, & \varepsilon^{SW} \leq \varepsilon_1^{SW} \\ \frac{\varepsilon^{SW} - \varepsilon_1^{SW}}{\varepsilon_2^{SW} - \varepsilon_1^{SW}}, & \varepsilon_1^{SW} < \varepsilon^{SW} < \varepsilon_2^{SW} \\ 1.0, & \varepsilon_2^{SW} \leq \varepsilon^{SW} \end{cases} \qquad [76]$$

where ε^{sw} is the calculated gas swelling and ε_1^{sw} is the threshold gas swelling for open pore formation. The breakaway swelling level ε_2^{sw} was taken as $\varepsilon_2^{sw} = 0.33$ based on a theoretical consideration by Barns.[65] The value of ε_1^{sw} can be determined either by irradiation experiences or by thermodynamic assessment of open pore morphology, as in the case of UO_2 fuel.[66] Tsai et al.[67] reported that fuel pins of 85% smear density, where the fuel slug is allowed to swell

only 18% before the slug–cladding contact, achieved 10 at.% peak burnup without cladding failure and showed a fractional fission gas release of ~60%. This suggests that the value of ε_1^{sw} should be much less than 0.18 (=18%). Based upon this irradiation experience, ε_1^{sw} is set to 0.10.

3.23.4.2.3.2.3 Fission gas release The amount of fission gas retained in a unit volume of the fuel alloy is expressed as

$$M_{retain} = C_g + C_{gb} + \sum_{i=1}^{M-1} m_i C_i \qquad [77]$$

and fission gas release during a time interval Δt is calculated from the change in the retained gas amount. Consistent with eqn [77], fission gas release rate $dM_{release}/dt$ can also be derived from eqn [69] multiplied by 'virtual' gas amount m_M in the open pore, namely,

$$\frac{dM_{release}}{dt} \equiv m_M \frac{dC_M}{dt} = m_M G_M + m_M \sum_{j=1}^{M-1} R''_{M-1,j}$$
$$+ m_M \sum_{j=1}^{M-1} R'_{M,j} \qquad [78]$$

The first term in eqn [78] represents release of the fission gas atom from the grain through the existing open pores. The second term means gas release when the grain-boundary (closed) bubbles are interconnected. The third represents release of the gas in the grain-boundary bubbles through the existing open pores.

3.23.4.2.3.2.4 Gas swelling Volumetric strain increment of the slug due to the closed bubble evolution during a time interval Δt is given by

$$\Delta \varepsilon_{n+1}^{cls} = \Delta t \sum_{i=0}^{M-1} v_i \frac{dC_i}{dt} \qquad [79]$$

where $i = 0$ means the intragranular bubble. The volume v_i of one class i bubble is calculated from the gas amount m_i in the bubble based on the Van der Waals equation. Volumetric strain increment due to open pore formation is given by

$$\Delta \varepsilon_{n+1}^{opn+} = v_M \frac{dC_M}{dt} \Delta t \qquad [80]$$

The open pore volume v_M is calculated by the expedient of using the same scheme as the closed bubbles.

3.23.4.2.4 Effect of radial cracks

After the fuel slug comes into contact with the cladding, further axial growth is restrained. The slug

deformation before the slug–cladding contact is anisotropic; The U–Zr binary fuels of about 75% smear density show an axial elongation of 8–10% of as-fabricated slug length, while radial growth is about 16% at the slug–cladding contact.[45] This anisotropic deformation can be related to the tearing at the grain or phase boundaries in the peripheral region of the slug due to anisotropic irradiation growth of α-U crystals.[7,45] In the case of the U–Pu–Zr ternary fuel, more pronounced anisotropy was observed and suggested to be dependent upon the Pu content and radial temperature gradient in the fuel slug.[45] The anisotropy of the ternary fuel slug can be attributed to large radial crack formation due to the brittle nature of the ternary slug.[45] The cracks increase the slug radial strain and promote the anisotropy. In order to incorporate the effect of the cracks on the stress–strain state, the concept of the effective slug radius was introduced. The effective radius r^{eff} is defined (see **Figure 26**) as

$$r^{eff} = r_0 + dr^{slug} + dr^{crack} = r^{slug} + dr^{crack} \qquad [81]$$

where r_0 is the as-fabricated slug radius, and dr^{slug} is the radial strain increment due to thermal expansion, elasticity, creep, gas, and solid FP swelling. The increment dr^{crack} is due to the cracks and the tearing. After the slug including the tears and cracks comes into contact with the cladding, swelling into the tears and cracks will occur. In fact, extrusion of inner zone fuel into the radial crack was observed.[45] This process will relax radial FCMI stress. During this stage of the contact (Stage II in **Figure 26**), the area of the contact interface continues to increase without significant FCMI stress, and then the slug will stick to the cladding. Using r^{eff}, the following contact conditions are adopted in the ALFUS calculation (see **Figure 26**);

(I) $r^{eff} < r_i$: no restraint by the cladding (no contact),
(II) $r^{slug} < r_i \leq r^{eff}$: axial restraint by the cladding, but no radial restraint,
(III) $r_i \leq r^{slug}$: both axial and radial restraints by the cladding,

where r_i is the inner radius of the cladding. When the aforementioned condition is applied to the contact-state judgment, the value of the anisotropic radius increment dr^{crack} at the beginning of Stage II ($r^{eff} = r_i$) must be known, which is estimated as follows.

As shown in Ogata,[53] the sum of the strain components except tearing and crack strains is almost isotropic until the slug–cladding contact, so that its strain vector can be expressed as $\{\varepsilon^{iso}, \varepsilon^{iso}, \varepsilon^{iso}\}$. Assuming that the sum of the tearing and crack
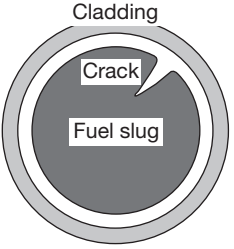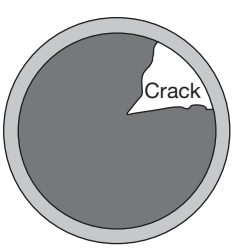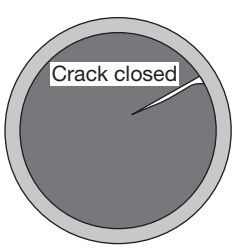
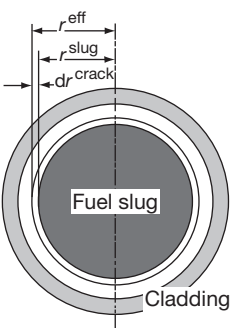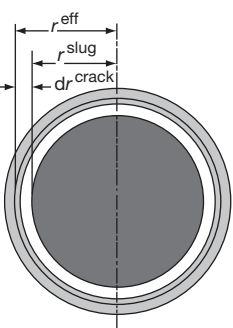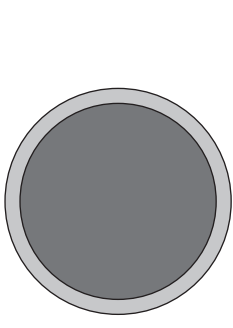| Stage of the slug–cladding contact	(I)	(II)	(III)
Actual fuel being irradiated:	Cladding / Crack / Fuel slug	Crack	Crack closed
Fuel being calculated by ALFUS:	r^{eff} / r^{slug} / $\mathrm{d}r^{\text{crack}}$ / Fuel slug / Cladding	r^{eff} / r^{slug} / $\mathrm{d}r^{\text{crack}}$	
Calculational condition at the outer surface of the slug:	No restraint	Axial restraint, but no radial restraint	Both axial and radial restraint

Figure 26 Calculation conditions of the slug–cladding contact-state.

strains is highly anisotropic and can be expressed as $\{\varepsilon^{\text{crack}}, \varepsilon^{\text{crack}}, 0\}$ (no axial component), local axial elongation can be expressed as $100\varepsilon^{\text{iso}}$ (%), and

$$\mathrm{d}r^{\text{slug}} = \varepsilon^{\text{iso}} r_0^{\text{slug}}, \mathrm{d}r^{\text{crack}} = \varepsilon^{\text{crack}} r_0^{\text{slug}} \qquad [82]$$

Here, the anisotropy factor f^{crack} is introduced, which is defined as a ratio of the anisotropic strain to the total strain at the slug–cladding contact ($r^{\text{eff}} = r_i$):

$$f^{\text{crack}} \equiv \left(\frac{\varepsilon^{\text{crack}}}{\varepsilon^{\text{iso}} + \varepsilon^{\text{crack}}} \right)_{\text{contact}} \qquad [83]$$

where variables in the parentheses $()_{\text{contact}}$ take the values at the slug–cladding contact. The anisotropy factor f^{crack} is assumed to be a function of the initial Pu content C_{Pu} and the temperature gradient in the peripheral region of the slug. The temperature gradient can be shown to be proportional to the value of q/D_0: the liner power rate divided by the diameter of the slug. Substitution of eqns [81] and [82] into [83] yields

$$\left(\mathrm{d}r^{\text{crack}}\right)_{\text{contact}} = f^{\text{crack}} r_0^{\text{gap}} \qquad [84]$$

where $r_0^{\text{gap}}(= r_i - r_0^{\text{slug}})$ is the initial gap width between the slug and cladding. The factor f^{crack} can be estimated as follows; eqn [83] can be transformed to

$$f^{\text{crack}} = 1 - \left(\frac{\varepsilon^{\text{iso}}}{\varepsilon^{\text{iso}} + \varepsilon^{\text{crack}}} \right)_{\text{contact}}$$

$$= 1 - \frac{\left(\varepsilon^{\text{iso}}\right)_{\text{contact}}}{\sqrt{\frac{100}{SD}} - 1} \qquad [85]$$

where SD is the initial smear density (%) of the fuel pin;

$$SD = \left(\frac{r_0^{\text{slug}}}{r_i} \right)^2 100 \qquad [86]$$

Values of f^{crack} for various fuel pins were calculated by using eqn [85], and plotted in **Figure 27** as a function of C_{Pu} and q/D_0. Values of $\left(\varepsilon^{\text{iso}}\right)_{\text{contact}}$ in eqn [85] were estimated from the experimental data[45,68,69] of the axial elongation of the whole slug instead of the local elongation. As can be seen in **Figure 27**, f^{crack} values saturate at $f^{\text{crack}} \approx 0.8$ when $C_{\text{Pu}} \geq 19$ (wt%) and $q/D_0 \geq 750$ (W cm^{-2}). In the calculations described
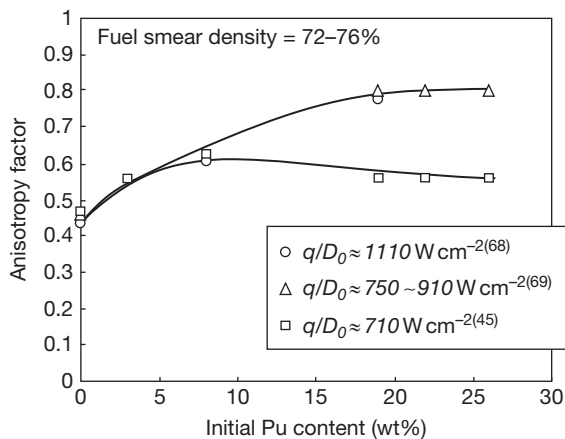
Figure 27 Anisotropy factor as a function of the Pu content and the temperature gradient.

in the next section, f^{crack} is set to 0.8 because C_{Pu} and q/D_0 for the analyzed fuel pins are within the above saturation range. The appropriate value of $\left(\mathrm{d}r^{crack}\right)_{contact}$ for each fuel pin is given by eqn [84].

The tearing model[53] is not used in the current version of ALFUS since the tearing strain is included in the concept of the effective slug radius introduced above.

3.23.4.2.5 Solid FP swelling model

Nongaseous FPs cause incompressible volume increase of the fuel slug, which is called 'solid FP swelling' hereinafter. The solid FP swelling in the metal fuel slug can be assumed to be proportional to burnup. Hence, isotropic strain increment $\Delta\varepsilon^{sol}$ due to the solid FP swelling is given in ALFUS by

$$\Delta\varepsilon^{sol} = \dot{\varepsilon}^{sol}\Delta Bu \qquad [87]$$

where $\dot{\varepsilon}^{sol}$ is volumetric strain increment per atomic percent burnup (at.%) due to the solid FP swelling, and ΔBu burnup increment. Hofman and Walters[1] gave a value of 1.2% per at.% to $\dot{\varepsilon}^{sol}$ by considering possible forms of non-gaseous FPs in the irradiated fuel alloy. Pahl et al.[70] estimated it as $\dot{\varepsilon}^{sol} = 1.68\%$ per at.% from the analyses of cladding strain data of irradiated fuel pins. The maximum value of solid FP swelling rate $\dot{\varepsilon}^{sol}$ can be obtained on the basis of the following theoretical consideration.

Some nongaseous FPs may form solid solution or intermetallic compounds with the fuel alloy constituents, and others may precipitate. Here, molar volume of each FP element in the fuel alloy matrix is simply assumed to be equal to that of the pure

substance. Table 6 summarizes the volume occupied by major FPs generated by one mole fissions of the heavy metals (U and Pu). The yield of each nuclide was calculated using a computer code ORI-GEN-2.[71] The one-group cross-sections used in the ORIGEN-2 code were generated with the neutron spectrum in the reactor core consisting of the U–Pu–10 wt% Zr ternary alloy fuel. As shown in Table 6, one mole fissions of the heavy metals lead to a net volume increase of 25.4 cm^3. This corresponds to a volumetric strain increment of 1.5% per 1 at.% burnup. Therefore, a solid FP swelling rate of $\dot{\varepsilon}^{sol} = 1.5\%$ per at.% was used in the ALFUS calculation presented in Section 3.23.4.3.

3.23.4.2.6 Correlation of cladding wastage by rare-earth FPs

As stated in the Introduction, rare-earth FPs attack the cladding and a wastage layer is formed at the inner surface of the cladding. This cladding wastage is called FCCI (fuel–cladding chemical interaction) hereinafter. It is essential to incorporate FCCI into the consideration of the cladding integrity. The mechanistic model for FCCI applicable to a wide range of the irradiation condition is too difficult to be constructed because the mechanism of FCCI has not been determined well at this stage. In the postirradiation examination, some traces of radial migration of rare-earth FPs were observed, and rare-earth-rich layer was found in the FCCI zone. Related data to quantify these phenomena are, however, not sufficient. Although the Pu content in the fuel slug, linear power rate of the fuel pin, etc., may affect FCCI behavior, these effects are not clear until now. Therefore, empirical correlation for FCCI was made for the ALFUS code. Assuming that FCCI is controlled by the solid-state diffusion mechanism and local burnup can be taken as a time-variable instead of the actual time, the cladding wastage increment $\Delta\delta$ during local burnup increment ΔBu is expressed as

$$\Delta\delta = \sqrt{K\Delta Bu} \qquad [88]$$

The rate constant K is obtained by fitting eqn [88] to the reported experimental data,[66,72,73] as follows:

$$K = 1.069 \times 10^{13}\mathrm{e}^{-20\,000/T} \qquad [89]$$

3.23.4.2.7 Temperature calculation model

An axial symmetric, r–z 2D finite element method is applied to calculation of the temperature distribution in the fuel slug and cladding. The crucial factors that affect the temperature distribution are changes in

Table 6   Amounts and volumes of major FPs generated by 1 mol fissions

	Elements	Generation (mol)	Molar volume (cc mol^{-1})	Volume change (cc)
Fuel	Zr	0.0000	14.01	0.00
constituents	U and Pu	−1.0000	12.58	−12.58
Fission products	(Noble gas)	(0.2518)		(−)
	Kr	0.0190		−
	Xe	0.2328		−
	(Alkali metals)	(0.2051)		(14.12)
	Rb	0.0162	55.86	0.90
	Cs	0.1890	69.95	13.22
	(Alkaline earth)	(0.1057)		(3.83)
	Sr	0.0340	33.32	1.13
	Ba	0.0718	37.62	2.70
	(Te and I)	(0.0559)		(1.25)
	Te	0.0354	20.42	0.72
	I	0.0205	25.69	0.53
	(Lanthanides)	(0.4499)		(9.44)
	Y	0.0181	19.89	0.36
	La	0.0561	22.55	1.26
	Ce	0.1002	20.70	2.07
	Pr	0.0515	21.75	1.12
	Nd	0.1614	20.61	3.33
	Pm	0.0052	20.08	0.11
	Sm	0.0469	19.94	0.94
	Eu	0.0054	28.95	0.16
	Gd	0.0051	19.93	0.10
	(Others)	(0.9260)		(9.32)
	Zr	0.1857	14.01	2.60
	Nb	0.0000	10.83	0.00
	Mo	0.2142	9.33	2.00
	Tc	0.0548	8.53	0.47
	Ru	0.1960	8.12	1.59
	Rh	0.0588	8.29	0.49
	Pd	0.1610	8.85	1.43
	Ag	0.0166	10.28	0.17
	Cd	0.0167	13.01	0.22
	In	0.0013	13.29	0.02
	Sn	0.0166	16.24	0.27
	Sb	0.0045	16.70	0.07
Net volume change				25.39

thermal conductivity of the slug due to evolution of the gas bubble and infiltration of the bond sodium. The thermal conductivity of the fission gas in the closed bubble and the open pore is much less than that of the fuel alloy, so that the effective conductivity of the irradiated slug is degraded as fractions of the bubbles and open pores increase. On the other hand, Hofman and Walters[1] reported that the bond sodium infiltrates the irradiated slug, probably through the open pore. Since the thermal conductivity of sodium is comparable to that of the U–Pu–Zr alloys, bond sodium infiltration recovers the degraded conductivity of the irradiated slug. These effects should be incorporated into the effective thermal conductivity of the slug.

Using the conductivity correction factor f_{con}, the effective thermal conductivity of the fuel slug is expressed[17] as

$$k_{eff} = f_{con} k_f \qquad [90]$$

where k_f is the thermal conductivity of the unirradiated fuel alloy. The correction factor f_{con} is approximated by the following expression,[17] which was derived for spherical gas-filled and irregular sodium-filled pores:

$$f_{con} = \left[1 - 3 \cdot \frac{P_{Na}}{1 - P_g} \cdot \frac{1 - \dfrac{k_{Na}}{k_f}}{\dfrac{2}{\varepsilon} + \left(3 - \dfrac{2}{\varepsilon} \right) \dfrac{k_{Na}}{k_f}} \right] \cdot \left(1 - P_g \right)^{3/2} \quad [91]$$

where k_{Na} is thermal conductivity of sodium, P_g volume fraction of gas-filled pore, and P_{Na} is the volume fraction of sodium-filled pore. The shape factor ε is taken as $\varepsilon = 1.72$. In the ALFUS model, a part of the existing open pores is assumed to be infiltrated by the bond sodium. Using the volume fraction F_N of the sodium-filled open pores to the total open pores, the volume fractions P_g and P_{Na} are expressed as

$$P_g = \frac{\varepsilon^{cls} + (1 - F_N)\varepsilon^{opn}}{1 + \varepsilon^{total}} \qquad [92]$$

$$P_{Na} = \frac{F_N \varepsilon^{opn}}{1 + \varepsilon^{total}} \qquad [93]$$

In eqns [92] and [93], ε^{total} denotes the total volumetric strain of the slug, ε^{cls} is volumetric strain due to the closed bubbles, and ε^{opn} volumetric strain due to the open pores. The volume fraction F_N is estimated as $F_N = 0.5$. As shown in the next section (**Figure 37**), the open pores occupy ~20–70% of the porosity: the volume fraction of the sum of the closed bubbles and the open pores to the swelled fuel. It means that about 10–35% of the porosity is assumed to be infiltrated by the bond sodium. This estimation is consistent with the following observation results: ~15–20% of the porosity[1] and 21–39% of the porosity[17] (calculated from Table I in Bauer and Holland[17]) are infiltrated by the sodium.

The thermal conductivity k_f of the unirradiated U–Pu–Zr alloy is given as a function of Pu content C_{Pu}, Zr content C_{Zr}, (in atom fraction), and temperature T (K);

$$k_f = 16.309 + 0.02713\,T - 46.279\,C_{Zr} \\ + 22.985\,C_{Zr}^2 - 53.545\,C_{Pu} \qquad [94]$$

This correlation was made by fitting the experimental data for the U–Zr alloys[74–76] and for the U–Pu–Zr alloys.[77]

3.23.4.2.8 Adjustment of the model parameters in ALFUS

Based on the theoretical and/or empirical considerations, the following key parameters were determined:

α: the hot press parameter for the open pore volume decrease (**Section 3.23.4.2.2**),
ε_1^{sw}: the threshold gas swelling for open pore formation (**Section 3.23.4.2.3**),
f^{crack}: the anisotropy factor in the crack model (**Section 3.23.4.2.4**), and
$\dot{\varepsilon}^{sol}$: the solid FP swelling rate (**Section 3.23.4.2.5**),

although values or correlations for these parameters include uncertainties due to effects of the various factors not considered in the models.

The models in ALFUS include other parameters and fuel alloy properties, values of which were assumed tentatively because of the lack of relevant data. The diffusion coefficient D_g of the gas atom was assumed to be equal to the self-diffusion coefficient of γ-uranium (eqn [59]). The larger number of the bubble class M is preferable to simulate the actual evolution of the bubbles, but $M = 6$ was assumed to cut down the computing time. The gas amounts m_i of the closed bubbles were determined as $m_1 = 4.0 \times 10^{-21}$, $m_2 = 1.6 \times 10^{-19}$, $m_3 = 6.4 \times 10^{-18}$, $m_4 = 2.6 \times 10^{-16}$, and $m_5 = 1.0 \times 10^{-14}$, because the observed bubble size is on the order of micron meter. In this case, the bubble radii of class 1 to $M-1$ are in the range of ~4 nm–1 µm. The diffusion coefficients D_i of the grain-boundary bubbles were assumed to be given by eqn [60] because of insufficient knowledge of the bubble mobility on the boundary.

On the premise that the tentative values and correlations mentioned earlier are used, values of the multiplication factor C_{adj} for the bubble diffusion coefficient (eqn [60]) and the parameter m_M ('gas amount' of the open pore; eqn [73]) were adjusted, as follows. Fission gas release data (**Figure 28**) show sharp increase in the amount of the gas released after an incubation period (~1 at.% peak burnup). At the higher burnup, the gas release levels off at an asymptotic value of ~60–80%. The calculated gas release over the whole irradiation period increases with the value of the factor C_{adj}, because a larger value of C_{adj} increases the collision and growth rate of the bubbles.
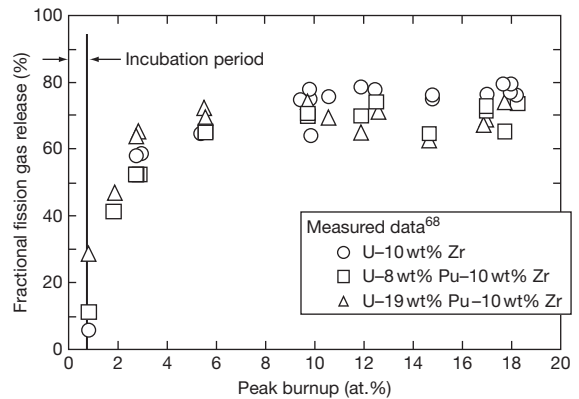

Figure 28 Fission gas release data[68] measured for ~72% smear density pins of the lead test assemblies.

On the other hand, the parameter m_M has an influence on the increasing rate of the gas release at the early stage of irradiation. At this stage, the second term in the right-hand side of eqn [69] is dominant compared to the other terms, and varies sensitively with a value of m_M as expected from eqns [71] and [74]. As a result of the calculations by ALFUS for various values of C_{adj} and m_M, $C_{adj} = 20$ and $m_M = 1.015 \times 10^{-14}$ were appropriate to simulate the measured data presented in **Figure 28**. If values or correlations of D_g, D_i, M, and m_i are determined from theoretical and/or empirical considerations in the future, the adjusted values of C_{adj} and m_M should be revised.

At the present stage, each of the parameter values and the property correlations assumed tentatively cannot be validated separately. In order to validate the ALFUS code as a whole, therefore, the results of the code calculation are compared with the experimental data of the fuel irradiation behavior, which is the superposition of the various phenomena. The validation of the ALFUS code is described in the next section.

3.23.4.3 Validation of ALFUS

In order to validate ALFUS, calculations were performed for the U–19Pu–10Zr (in wt%) fuel pins of the EBR-II test assemblies designated as X425 and X441. The X425 assembly consisted of 72% smear density pins and was irradiated until the cladding breach occurred at ~19 at.%.[50,70] The X441 assembly, which included different smear density pins (70, 75, 85%), was irradiated up to ~10 at.% burnup.[70] The cladding material of both assemblies was the low-swelling martensitic steel, HT9. The values of the model parameters and fuel alloy properties discussed in **Section 3.23.4.2** are used in all the following ALFUS calculation. Specifications and irradiation conditions of the fuel pins analyzed in this section are summarized in **Table 7**.

3.23.4.3.1 Fission gas release

Fractional fission gas release calculated for the X425 fuel pin is shown in **Figure 29**. Release of fission gas starts at ~0.7 at.% peak burnup, which corresponds to the onset of interconnection of the closed bubbles (open pore formation), and levels off at higher burnup. This leveling-off behavior of the gas release is due to stable existence of the open pores over higher burnup as indicated later (**Figure 37**). **Figure 29** also shows the measured gas release data

Table 7   Specification and irradiation condition[70] of fuel pins analyzed in the present study

Assembly No.	X441[a]	X425
Cladding material	HT9	HT9
Clad outer diameter (nm)	5.84	5.84
Clad wall thickness (mm)	0.38	0.38
Fuel alloy composition (wt%)	U–19Pu–10Zr	U–19Pu–10Zr
Slug outer diameter (mm)	4.67	4.32
Fuel slug length (mm)	343	343
Smear density (%)	~85	~72
Peak linear power (W cm^{-1})	~510	~400
Peak cladding temp (°C)	~600	~590

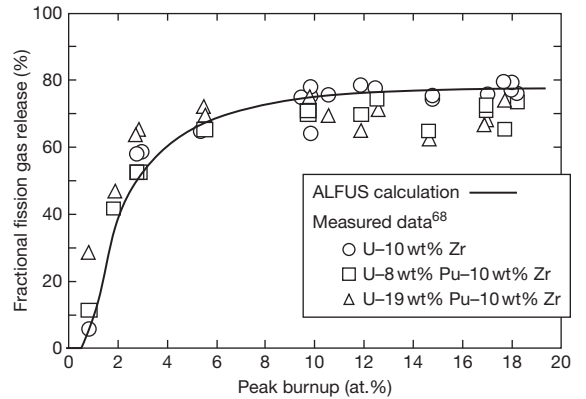[a]Listed only for 85% smear density pin although X441 includes different smear density pins.

Figure 29 Calculated result of fractional fission gas release for U–19Pu–10Zr (wt%) pin of X425 assembly: measured data[68] are from ~72% smear density pins of the lead test assemblies.

for ~72% smear density pins of the lead test assemblies designated X419, X420, and X421.[68] Although the gas release data for the X425 pins have not been published, Pahl *et al.*[70] reported that they are consistent with the lead test data. The calculated curve reasonably represents the trend of these measured data. The calculated burnup of the gas release onset (the incubation period) is related to the threshold gas swelling ε_1^{sw} for open pore formation and the gas swelling rate. The agreement between the calculated and test results as shown in **Figure 29** indicates that ALFUS calculates a reasonable level of the gas swelling rate.

3.23.4.3.2 Axial elongation of the fuel slug

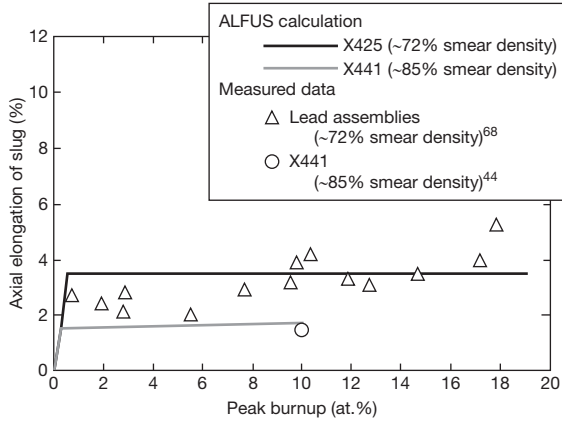The slug axial elongation calculated for the same X425 pin is shown in **Figure 30**, again in comparison

Figure 30 Calculated result of slug axial elongation of the X425 and X441 pins: measured data are from the fuel pins of the lead assemblies[68] and X441.[44]

with the measured data for the lead test assemblies. The result obtained for the 85% smear density pin of X441 is also shown in **Figure 30**. The calculated curves agree well with the measured data. The calculated slug elongation stops at the beginning of the slug–cladding contact stage II (**Figure 26**), so that the parameter f^{crack} is crucial to simulation of the axial elongation of the slug. Note that the data used to determine an appropriate value of f^{crack} do not include those of the X441 pins. The reasonable calculation of the gas swelling rate can be confirmed also by **Figure 30**.

3.23.4.3.3   Cladding diametral strain and FCMI
3.23.4.3.3.1   Axial distribution of cladding strain
The curves in **Figure 31** are the calculated axial distributions of the cladding diametral strain for the X425 pins at 10.4, 15.8, and 18.9 at.% peak burnup. As the swelling of HT9 steel was neglected in accordance with Yacout and Orechwa,[78] the calculated cladding strain in this section is essentially due only to irradiation creep. In ALFUS, the following correlation of irradiation creep strain rate $\bar{\varepsilon}$ for HT9 is used:

$$\bar{\varepsilon} = \bar{B}\sigma^{1.5}\phi t \qquad [95]$$

where σ is the equivalent cladding stress (MPa) and ϕt fast neutron fluence (n cm^{-2}). The following expression for the effective creep coefficient $\bar{B}$ is made by fitting the experimental data reported in Chin[79] and Puigh[80];

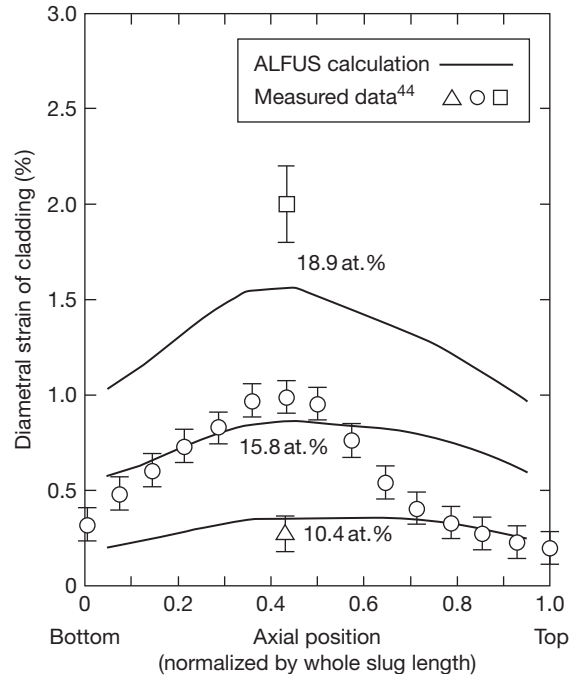$$\bar{B} = \frac{1.575 \times 10^{-26}}{923 - T} \qquad [96]$$

Figure 31 Calculated results and measured data[44] of cladding diametral strain at 10.4, 15.8, and 18.9 at.% peak burnup (X425, smear density ∼72%).

where T is cladding temperature (K). Each calculated strain curve in **Figure 31** has a maximum near the core mid-plane, although the effective creep coefficient is larger at the higher elevation of the cladding where the temperature is higher. This shape of the cladding strain curve is attributed not only to neutron flux distribution similar to the chopped-cosine but also to axial distribution of FCMI stress. **Figure 32** shows the calculated FCMI stress distributions for the X425 pins at 10.4, 15.8, and 18.9 at.% peak burnup. The volume decrease of the open pores, which accommodates the closed bubble swelling and the solid FP swelling, is slower at the lower (colder) part of the slug where the creep strain rate of the slug is smaller. Therefore, FCMI stress is larger at the lower part of the cladding, despite the axial distributions of the closed bubble and the solid FP swelling rates, which are proportional to the linear power rate. As a result of the combined effects of FCMI, uniform plenum gas pressure, neutron flux distribution, and cladding temperature, the calculated cladding strain shows the aforementioned distribution.

Figure 31 also shows the measured strain data,[44] which indicate that the cladding strain increases significantly after ∼10 at.% burnup. The ALFUS calculation qualitatively reproduces the data trend,
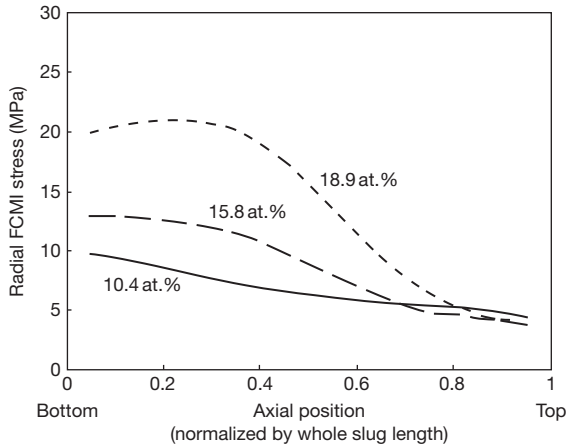
Figure 32 Calculated result of FCMI stress (X425, smear density ~72%) at different peak burnup.

although the calculation overpredicts the data at the top part of the 15.8 at.% burnup pin. The results for the X441 pins of 85% smear density are shown in **Figure 33**, where large cladding strain was observed for the 10 at.% burnup pins. The calculated curves (thick solid lines) in **Figure 33** generally agree with the measured data although slight overpredictions occur for both the top and bottom parts of the 10 at.% burnup pins. Similar discrepancies between measured and calculated results are also observed in the LIFE-METAL code predictions,[70] and can be attributed to uncertainties in the irradiation condition and mechanical properties of HT9, as pointed out in Pahl *et al.*[70] Considering these uncertainties, it can be concluded that the cladding strain calculations shown in **Figures 31** and **33** agree approximately with the measured data.

3.23.4.3.3.2 Dependency of cladding strain on fuel smear density

In **Figure 34**, the measured data[70] of the maximum cladding diametral strain for the X441 pins are plotted against the smear density, together with the ALFUS calculation results. The ALFUS results agree well with the measured data. The large strains observed in the case of the 85% smear density pins at the higher burnup (1.25 full power years) are caused by a significant level of FCMI. This dependency of the cladding strain on the smear density can be clearly explained by the detailed history of the fuel slug swelling shown in **Figures 35** and **36**, where the radially averaged swelling components at an axial position near the core mid-plane are plotted against burnup. In the case of 85% smear density (**Figure 35**),
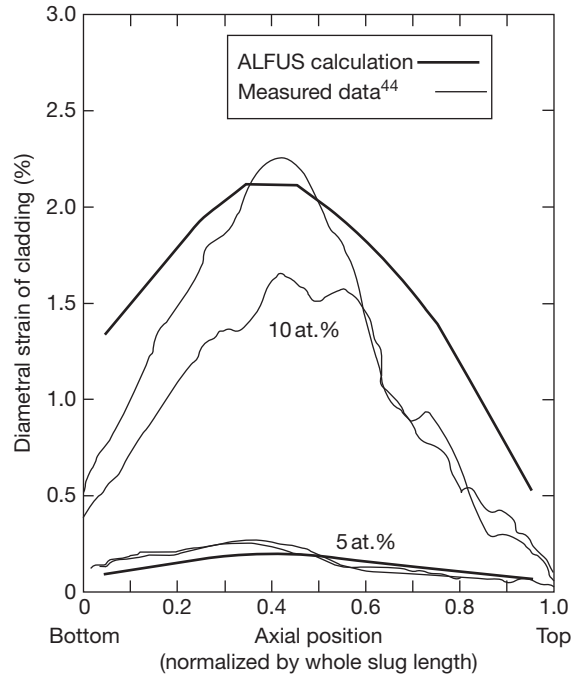

Figure 33 Calculated results and measured data[44] of cladding diametral strain at 5 and 10 at.% peak burnup (X441, smear density ~85%).
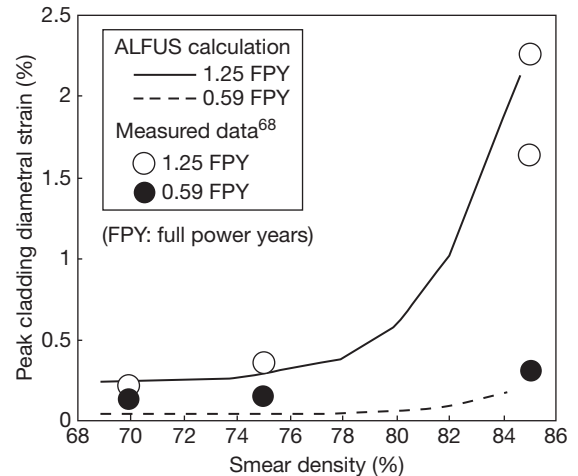

Figure 34 Dependency of peak cladding diametral strain on fuel smear density (X441 assembly).

swelling due to the open pores is only ~5% at ~1 at.% burnup when the initial slug–cladding gap is filled with the swollen slug. At the latter stage of irradiation, the open pore volume is replaced by the solid FP swelling, and becomes insufficient to accommodate further solid FP swelling. It leads to continuous
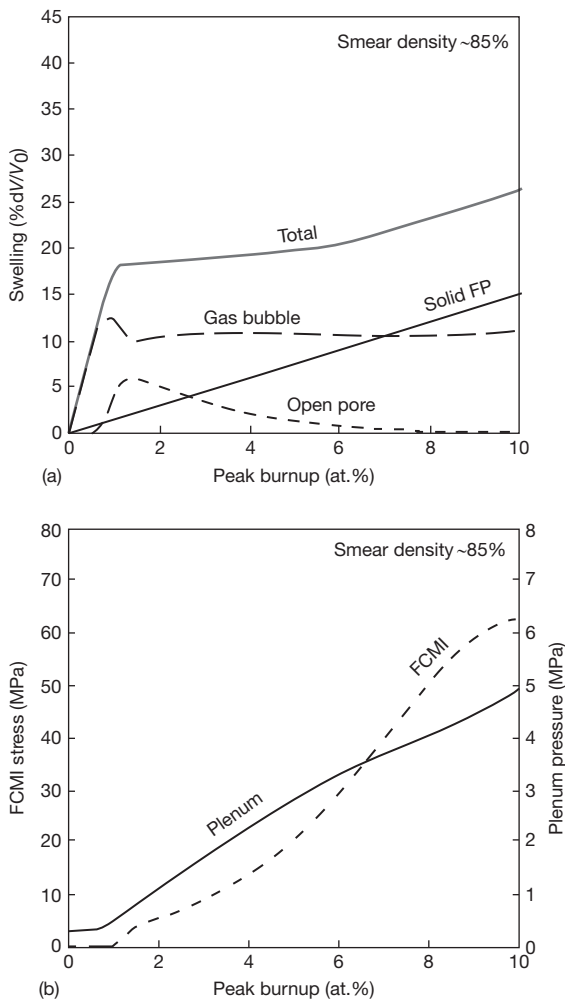
Figure 35 Calculated histories of (a) radially averaged swelling components and (b) FCMI stress and plenum pressure at the axial position of 45% of the slug length from the bottom (X441, smear density ~85%).

Figure 36 Calculated histories of (a) radially averaged swelling components and (b) FCMI stress and plenum pressure at the axial position of 45% of the slug length from the bottom (X441, smear density ~75%).

increase in FCMI stress as indicated in **Figure 35(b)**. In the case of lower smear density (**Figure 36**), the open pore swelling amounts to more than 20%, and can serve as a buffer against the solid FP swelling. Consequently, FCMI stress remains at a low level up to 10 at.% burnup (**Figure 36(b)**).

3.23.4.3.3.3   Effect of solid FP accumulation at higher burnup

At a very high burnup, significant FCMI can occur even in the case of low smear density pins because of the accumulation of the solid FPs. This effect of the solid FP swelling at higher burnup is illustrated in **Figure 37**, which shows the calculated swelling history in the very high burnup pin of the X425 assembly.

In this case, although decrease in the open pore volume accommodates the solid FP swelling until ~13 at.% burnup, the remaining volume of the open pores becomes too small at the higher burnup. This leads to significant increase in the FCMI stress as indicated in **Figure 37(b)**. This mechanism explains the increase in the measured cladding strain data after ~10 at.% burnup, which is shown in **Figure 31**.

3.23.5   Summary and Outlook

The constituent migration model and the simulation codes LIFE-METAL and ALFUS are capable of simulating metal fuel irradiation behavior to some
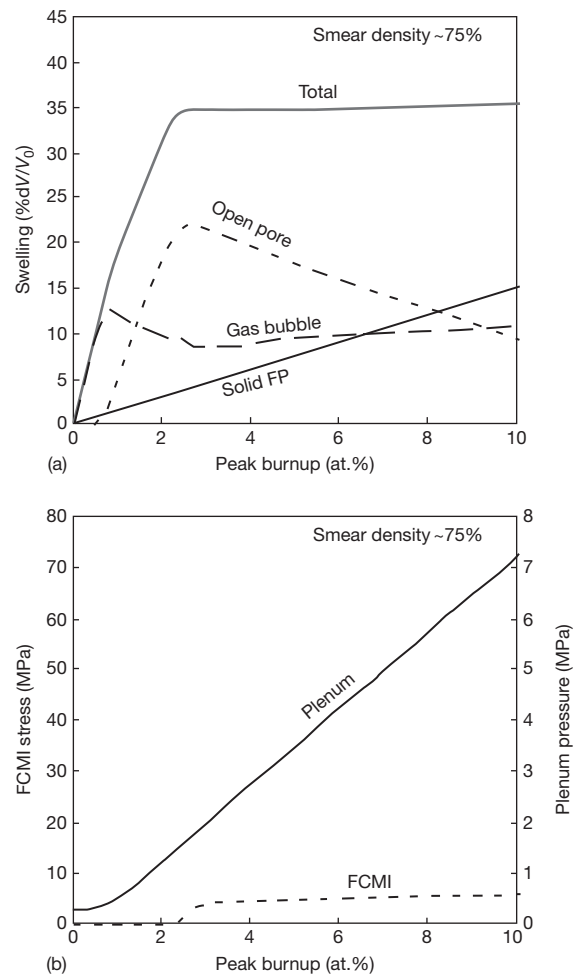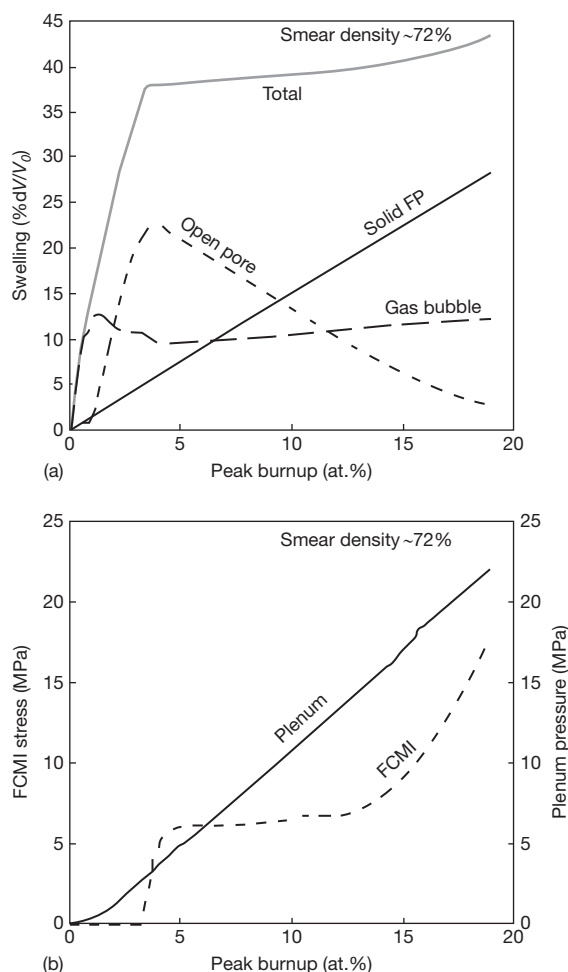
Figure 37 Calculated histories of (a) radially averaged swelling components and (b) FCMI stress and plenum pressure at the axial position of 45% of the slug length from the bottom (X425, smear density ~72%).

extent. Improvements in the models and codes are recommended with respect to the following points:

- Incorporation of the swelling models for respective annular zones formed in the fuel slug corresponding to α-uranium zone, intermediate zone, and γ-uranium zone.
- Coupling of the fuel constituent migration model and swelling models, then introducing them into a comprehensive simulation code, after measurement of dependency of fuel alloy mechanical properties on the composition.
- Measurement of compressibility data of porous metal fuel alloy.
- Evaluation of the solid FP swelling rate based on the analysis of the forms of FPs in the fuel alloy.

- Understanding of radial migration of rare-earth fission products and FCCI.

In the future, the progress in the development of the reprocessing of irradiated metal fuel may lead to increased interest in the metallurgical or chemical behavior of actinides and FPs in metal fuel pins. The migration of rare-earth FPs into the cladding, accompanied by actinides, will affect actinide recovery of the process and radioactivity of the cladding waste. The forms of noble metal FPs in a metal fuel pin will be important in the evaluation of the amount of anode slime in the electrorefining process, as well as in the evaluation of solid FP swelling. Parts of alkali and alkaline earth FPs migrate to the gas plenum region through bond sodium, which will affect radioactivity of the cladding waste.

For a better understanding of metal fuel irradiation behavior and to improve the models and codes, it is essential to conduct more irradiation tests and accumulate physical and thermochemical property data. Out-of-pile tests for a simplified or idealized system are also useful for modeling. The authors are hopeful about significant progress in metal fuel modeling and simulation in the near future.

References

1. Hofman, G. L.; Walters, L. C. In *Material Science and Technology, A Comprehensive Treatment*; Cahn, R. W., Haasen, P., Kramer, E. J., Eds.; VCH Verlagsgesellschaft: Weinheim, Germany, 1994; Vol. 10A.
2. Billone, M. C.; *et al.* In *Proceedings of the International Conference on Reliable Fuels for Liquid Metal Reactors*, Tucson, AZ, Sept 7–11, 1986; American Nuclear Society: La Grange Park, IL.
3. Ogata, T.; Yokoo, T. *Nucl. Technol.* **1999**, *128*, 113.
4. Hwang, W.; *et al. Nucl. Technol.* **1998**, *123*, 130.
5. Karahan, A.; Buongiorno, J. *J. Nucl. Mater.* **2010**, *396*, 283–293.
6. Kim, Y. S.; Hofman, G. L.; Hayes, S. L.; Yacout, A. M. *J. Nucl. Mater.* **2006**, *359*, 17.
7. Rest, J. *J. Nucl. Mater.* **1993**, *207*, 192.
8. Murphy, W. F.; Beck, W. N.; Brown, F. L.; Koprowski, B.; Neimark, L. A. Postirradiation examination of U–Pu–Zr fuel elements irradiated in EBR-II to 4.5 atomic percent burnup, Report ANL-7602; Argonne National Laboratory, 1969.
9. Harbur, D. R.; Anderson, J. W.; Maraman, W. J. Studies on the U–Pu–Zr alloy system for fast breeder reactor application, Report LA-4512; Los Alamos Scientific Laboratory, 1970.
10. Pahl, R. G.; Lahm, C. E.; Villareal, R.; Beck, W. N.; Hofman, G. L. Recent irradiation tests of uranium–plutonium–zirconium metal fuel elements. In *Proceedings of the International Conference on Reliable Fuels for Liquid Metal Reactors*, Tucson, AZ, Sept 7–11, 1986; pp 3–36.

11. Pahl, R. G.; Porter, D. L.; Lahm, C. E.; Hofman, G. L. *Metall. Trans. A* **1990**, *21A*, 1863.
12. Porter, D. L.; Lahm, C. E.; Pahl, R. G. *Metall. Trans. A* **1990**, *21A*, 1871.
13. O'Boyle, D. R.; Dwight, A. E. In *Proceedings of the 4th International Conference on Plutonium and Other Actinides,* Santa Fe, NM; Material Society: New York, 1970; p 720.
14. Saunders, N.; Miodownik, A. P. In *CALPHAD, Calculation of Phase Diagrams: A Comprehensive Guide*; Cahn, R. W., Ed.; Pergamon Materials Series; Pergamon: Oxford, 1998; Vol. 1.
15. Kurata, M. *CALPHAD* **1999**, *23*(3–4), 305–337.
16. Andersson, J. O.; Helander, T.; Höglund, L.; Shi, P.; Sundman, B. *CALPHAD* **2002**, *26*(2), 273.
17. Bauer, T. H.; Holland, J. W. *Nucl. Technol.* **1995**, *110*, 407.
18. Ogawa, T.; Iwai, T. *J. Less-Common Metals* **1991**, *175*, 59.
19. Hofman, G. L.; Hayes, S. L.; Petri, M. C. *J. Nucl. Mater.* **1996**, *227*, 277.
20. Ishida, M.; *et al. Nucl. Technol.* **1993**, *104*, 37.
21. Marino, G. P. *Nucl. Sci. Eng.* **1972**, *49*, 93.
22. Meyer, M. K.; Hayes, S. L.; Crawford, D. C.; Pahl, R. G.; Tsai, H. In *Proceedings of ANS Conference on Accelerator Applications in the New Millennium*, Reno, NV, Nov 11–15, 2001.
23. Kim, Y. S.; Hofman, G. L.; Hayes, S. L.; Sohn, Y. H. *J. Nucl. Mater.* **2004**, *327*, 27.
24. Johansson, B. *Phys. Rev. B* **1975**, *11*, 1367.
25. ANL-IFR-169. Integral Fast Reactor Program Annual Progress Reports FY 1991, June 1992.
26. Jankus, V. Z.; Weeks, R. W. *Nucl. Eng. Des.* **1972**, *18*, 83.
27. Boltax, A.; *et al.* In *International Fast Reactor Safety Meeting*, Snowbird, UT, 1990; American Nuclear Society: Hinsdale, IL, 1990; Vol. II, pp 427–436.
28. Liu, Y. Y.; Zawadzki, S.; Billone, M. C.; Nayak, U. P.; Roth, T. Development of LIFE-4CN. In *Post-SMiRT5 Second International Seminar on Mathematical/Mechanical Modeling of Reactor Fuel Elements*, Berlin, Germany, Aug 20, 1979.
29. Chang, Y. I. *Nucl. Technol.* **1989**, *88*, 129.
30. Hughes, T. H.; Kramer, J. M. The FPIN2 Code – An application of the finite element method to the analysis of the transient response of oxide and metal fuel elements. In *Proceedings of Conference on Science and Technology Fast Reactor Safety*, Guernsey, UK, May 1986; 427.
31. Liu, Y. Y.; Tsai, H.; Billone, M. C.; Holland, J. W.; Kramer, J. M. *J. Nucl. Mater.* **1993**, *204*, 194.
32. Kramer, J. M.; Liu, Y. Y.; Billone, M. C.; Tsai, H. C. *J. Nucl. Mater.* **1993**, *204*, 203.
33. ANL-IFR-246. Integral Fast Reactor Program Annual Progress Reports FY 1994, Dec 1994.
34. Yacout, A. M.; Tsuboi, Y.; Ueda, N. Development of 4s and related technologies(2): Long life metallic fuel. In *Proceedings of ICAPP'09,* Tokyo, Japan, May 10–14, 2009; paper 9195.
35. Jankus, V. Z.; Weeks, R. W. LIFE-I: A Fortran-IV Computer Code for the prediction of fast reactor fuel element behavior, USAEC Report ANL-7736; Argonne National Laboratory, 1970.
36. Tsai, H. Fuel/cladding compatibility in irradiated metallic fuel pins at elevated temperatures. In *International Fast Reactor Safety Meeting*, Snowbird, UT, Aug 12–16, 1990.
37. Yacout, A. M.; Hofman, G. L.; Lambert, J. D. B.; Kim, Y. S. Fuel behavior modeling issues associated with future fast reactor systems. In *GLOBAL 2007: Advanced Nuclear Fuel Cycles and Systems*, Boise, ID, Sept 9–13, 2007.
38. Kim, Y. S.; Yacout, A. M.; Hofman, G. L.; Ryu, H. J. *Trans. Am. Nucl. Soc.* **2007**, *96*, 709.
39. ANL-IFR-244. Integral Fast Reactor Program Annual Progress Reports FY 1993, Oct 1994.
40. Leibowitz, L.; Blomquist, R. A.; Pelton, A. D. *J. Nucl. Mater.* **1991**, *184*, 59–64.
41. Nakamura, K.; Ogata, T.; Kurata, M.; Yokoo, T.; Mignanelli, M. A. *J. Nucl. Mater.* **2002**, *304*, 63–72.
42. Turchi, Private communication. Lawrence Livermore National Laboratory, 2008.
43. Kim, Y. S.; Hofman, G. L.; Yacout, A. M.; Turchi, P. In *Global 2009*, Paris, France, Sept 6–11, 2009.
44. Billone, M. C. Unpublished work, Argonne National Laboratory, 1994.
45. Hofman, G. L.; *et al. Metall. Trans.* **1990**, *21A*, 517.
46. Crawford, D. C.; Porter, D. L.; Hayes, S. L. *J. Nucl. Mater.* **2007**, *371*, 202.
47. Pahl, R. G.; Porter, D. L.; Crawford, D. C.; Walters, L. C. *J. Nucl. Mater.* **1992**, *188*, 3.
48. Yacout, A. M.; Salvatores, S.; Orechwa, Y. *Trans. Am. Nucl. Soc.* **1993**, *69*, 193.
49. Yang, W. S.; Yacout, A. M. Assessment of the SE2-ANL Code for EBR-II temperature predictions. In *Proceedings of the 7th International Meeting on Nuclear Reactor Thermal Hydraulics (NURETH-7)*, Saratoga Springs, NY, Sept 10–15; 1995; Vol. 3, p 2394.
50. Yacout, A. M.; Salvatores, S.; Orechwa, Y. *Nucl. Technol.* **1996**, *113*, 177.
51. Yacout, A. M.; Yang, W. S.; Hofman, G. L.; Orechwa, Y. *Nucl. Technol.* **1996**, *115*, 61.
52. Hill, R. N. Private communication, Argonne National Laboratory, 2006.
53. Ogata, T.; *et al. J. Nucl. Mater.* **1996**, *230*, 129.
54. Nakajima, T.; *et al.* Japan Atomic Energy Research Institute Report JAERI-M 9251, 1981.
55. Rashid, Y. R.; *et al. Nucl. Eng. Des.* **1974**, *29*, 1.
56. Gruber, E. E.; Kramer, J. M. In *13th International Symposium on Radiation-Induced Changes in Microstructure (Part I)*, ASTM STP 955, 1987; p 432.
57. McDeavitt, S. M. PhD Thesis, Purdue University, 1992.
58. Tsuboi, Y.; *et al. J. Nucl. Mater.* **1992**, *188*, 312.
59. Wood, M. H.; Matthews, J. R. *J. Nucl. Mater.* **1980**, *91*, 35.
60. Matthews, J. R.; Wood, M. H. *Nucl. Eng. Des* **1980**, *56*, 439.
61. Brandes, E. A., Ed. *Smithells Metals Reference Book*, 6th ed.; Butterworth: London, 1983.
62. Olander, D. R. *Fundamental Aspects of Nuclear Reactor Fuel Elements*, TID-26711-P1; US Technical Information Center, US ERDA: Springfield, VA, 1976.
63. Gruber, E. E.; Kramer, J. M. *J. Am. Ceram. Soc.* **1987**, *70*(10), 699.
64. Hayns, M. R.; Wood, M. H. *J. Nucl. Mater.* **1977**, *67*, 155.
65. Barns, R. S. *J. Nucl. Mater* **1964**, *11*, 135.
66. Beere, W.; Reynolds, G. L. *J. Nucl. Mater.* **1973**, *47*, 51.
67. Tsai, H.; *et al.* In *Proceedings of 3rd JSME/ASME Joint International Conference on Nuclear Engineering*, Kyoto, Japan, Apr 23–27, 1995; Vol. 2, p 849.
68. Pahl, R. G.; *et al.* In *Proceedings of International Fast Reactor Safety Meeting*, Snowbird, UT, 1990, American Nuclear Society: La Grange Park, IL, Vol. IV.
69. Crawford, D. C.; *et al. Trans. Am. Nucl. Soc.* **1994**, 71.
70. Pahl, R. G.; *et al.* In *Proceedings of International Conference on Fast Reactor and Related Fuel Cycles*, Kyoto, Japan, Oct 28–Nov 1, 1991; Atomic Energy Society of Japan: Tokyo, Japan.
71. Croff, A. G. ORNL/TM-7175, Oak Ridge National Laboratory, 1980.
72. Cohen, A. B.; *et al. J. Nucl. Mater.* **1993**, *204*, 244.
73. Pahl, R. G.; *et al. J. Nucl. Mater.* **1993**, *204*, 141.
74. Takahashi, Y.; *et al. J. Nucl. Mater.* **1988**, *154*, 141.

75. Argonne National Laboratory. Chemical Technology Division Annual Technical Report for 1986, ANL-87–19, 1987.
76. Touloukian, Y. S.; *et al.* Ed. *Thermal Conductivity, Metallic Elements and Alloys*; IFI/Plenum: New York, 1970; Vol. I.
77. Argonne National Laboratory. Reactor Development Progress Report, ANL-7230,1969.
78. Yacout, A. M.; Orechwa, Y. *Trans. Am. Nucl. Soc.* **1992**, *65*, 191.
79. Chin, B. A. In *Topical Conference on Ferritic Alloys for Use in Nuclear Energy Technologies*, Snowbird, UT, 1983; p 593.
80. Puigh, P. J. In *12th International Symposium on Effects of Radiation on Materials*, ASTM STP 870; 1985; p 7.